國立交通大學

電子工程學系

碩 士 論 文

以銅為基礎的超常介質之光學性質探討

Optical Studies of Cu-based Meta-materials

研 究 生：韓佩軒

指導教授：倪衛新　教授

中 華 民 國 九 十 六 年 八 月

以銅為基礎的超常介質之光學性質探討

Optical Studies of Cu-based Meta-materials

研 究 生：韓佩軒　　Student：Pei-Hsuan Han

指導教授：倪衛新　　Advisor：Prof. Wei-Xin Ni

國 立 交 通 大 學

電 子 工 程 學 系

碩 士 論 文

A Thesis

Submitted to Institute of Electronics

College of Electrical Engineering

National Chiao Tung University

in partial Fulfillment of the Requirements

for the Degree of

Master of Science

in

Electronics Engineering

August 2007

Hsinchu, Taiwan, Republic of China

中華民國九十六年八月

以銅為基礎的超常介質之光學性質探討

研究生：韓佩軒　　指導教授：倪衛新 教授

國立交通大學

電子工程學系 電子研究所碩士班

摘要

超常介質物質是由週期性排列的二維(或三維)的金屬圖形結構(或是為晶格)組成，蘊含有新奇的光學性質，例如：電漿子共振、人工磁性以及左手物質現象等，皆起因於某特定波長的電磁波(或是光)在沿著金屬陣列的表面傳遞時候，材料所呈現的負的導電係數(ε)、導磁係數（μ）及由此而造成負折射率現象。

本論文工作期間，採用以銅化學置換取代一般傳統銅電鍍的實驗方式，建立起一套圖形製程技術，成功地製造了線寬達到次微米的等級的三種銅基超常介質物質的圖形陣列：裂隙共振環(split ring resonator, SRR)、不連續導線(WIRE)以及組合式超常介質物質(composite meta-material, CMM, 由SRR和WIRE組成)，圖形陣列面積大約是 0.09cm^2。傅式光學轉換紅外線光譜儀(FTIR)被用於實驗研究超常介質物質圖案所產生的光學性質。通過改變入射光的偏極化特性，在 600-2000 cm^{-1}波數範圍內，在三種圖案上觀察到了由不同物理機制導致的多各共振模態。為了進一步深入探討這些銅基超常介質物質光學特性之物理內涵，我們亦採用CST MWS軟體按所設計製造的超常介質物質圖形作了電磁模擬，模型計算結果與實驗有較好的符合。

Optical Studies of Cu-based Meta-materials

Student: Pei-Hsuan Han Advisor: Prof. Wei-Xin Ni

Department of Electronics Engineering

and Institute of Electronics

National Chiao-Tung University

Abstract

Meta-materials are a group of periodically patterned two-dimensional (or even three-dimensional) metal structures (lattices), which reveal some novel optical properties, such as plasmonic resonance, artificial magnetism, and/or left-handed behaviors, due to existing negative values of permittivity (ε), permeability (μ), and consequent refraction index (n), when electromagnetic (EM) waves (light) propagating along the surface of these pattern arrays at a certain range of wavelengths.

By using copper (Cu) chemical replacement instead of electrochemical plating, a new fabrication technology has been developed through this thesis work, and been successfully used in producing Cu-based meta-materials with line-widths at the sub-micrometer-scale. Three types of pattern structures, namely, split ring resonator (SRR), discontinuous wires (WIRE) and composite meta-materials (CMM = SRR+WIRE) were designed and processed forming periodic arrays in the area of about 0.09 cm^2. Fourier transfer infrared spectroscopy (FTIR) measurements were engaged for the study of optical properties of these meta-material structures. Over the range of 600-2000 cm^{-1}, several resonance modes with different physics origins were observed from the spectra of three type patterns, when varying the polarization of incident light. EM simulations were also performed using a CST MWS solver for modeling the meta-material behavior at the corresponding wavelength range. Comparison with experiment results were made, in order to facilitate discussions of possible mechanism and physical insights of these Cu-based meta-materials.

Acknowledgement

I would like to express my sincere gratitude to my advisor professor Wei-Xin Ni, and Dr. Shich-Chuan Wu for their support and guidance on my research. They were kind in correcting my mistakes. I'd also give my thanks to engineers at NDL: Jing-Sian Chen, Yao-Jhen Chen, Bai-Yan Chen, Syu-Jyun Jheng, Jin-Cai Syu, and Zu-Rong Ge, who assisted me in various ways in solving problems during my thesis work. Besides, I am thankful to my friends: Bing-Sian Chen, You-Jhen Jhang, Shih-Ming You, Bing-Ruei Lyu, Guo-Jheng Jhang, and specially thanks to Feng-I Tai, for their assistance. It was wonderful having the chance to work with them all. Finally, I am deeply grateful to my parents for their support and love.

Contents

List of Table

List of Figure

Chapter 1

Introduction

Usually, optical materials have positive values of dielectric permittivity ε and magnetic permeability μ. The refractive index n could then be simply taken as $\sqrt{\varepsilon\mu}$. Although it was realized that the refractive index would have to be a complex quantity to account for absorption, and even a tensor to describe anisotropic behavior of materials, the question of the sign of the refractive index did not arise.

In 1976, Veselago [1] first considered the case of a medium that had both negative ε and μ. At a given frequency, he concluded that the medium should be considered to have a negative refractive index (i.e. the negative square root, $n=-\sqrt{\varepsilon\mu}$, had to be chosen). His result remained an academic curiosity for a long time, as real materials with simultaneously negative ε and μ were not available. During recent years, there has been a significantly increased interest, since theoretical proposals [2, 3] for structured photonic media whose ε and μ could become negative in certain frequency ranges were realized experimentally [4, 5]. This development thus brought the Veselago's result into limelight, and the field has then become a hot topic of scientific research.

1.1 Basic concepts and definitions

The dielectric permittivity (ε) and the magnetic permeability (μ) characterize the macroscopic response of a homogeneous medium to apply electric and magnetic fields. These are macroscopic parameters because one usually only seeks time- and spatial-responses that were averaged over sufficiently long times and sufficiently large spatial volumes. All that survives the averaging in macroscopic measurements are the frequency components of the individual (atomic or molecular) oscillators driven by the external fields. This idea can now be extended to a higher class of inhomogeneous materials where the inhomogeneities were in length-scales much smaller than a wavelength of the radiation, but can be compared with atomic or molecular length-scales. The radiation then does not resolve these individual mesostructures, but responds to the (atomically) macroscopic resonances of the structure. Such materials have been named meta-materials [6, 7]. And could be characterized by macroscopic parameters such as ε and μ that define their response to applied electromagnetic fields, much like homogeneous materials.

Consider the Maxwell's equation for a planar harmonic wave $\exp[i(\mathbf{k}\cdot\mathbf{r}-\omega t)]$:

$$\mathbf{k}\times\mathbf{E}=\omega\mu_0\mu\mathbf{H}, \tag{1.1}$$

$$\mathbf{k}\times\mathbf{H}=-\omega\varepsilon_0\mathbf{E}, \tag{1.2}$$

where **E** and **H** are the electric and magnetic fields, respectively. If we take a medium with negative real parts of ε and μ with the imaginary parts being small (negligibly small for the time being) at some frequency (ω), then we realize that the vectors **E**, **H** and **k** will form a left-handed triad. It is for this reason that such materials are also popularly termed as left-handed materials, although this does risky confusion with the terminology of chiral optical materials. Using the definition that the wave-vector $\mathbf{k}=(n\omega/c)\hat{n}$, where $\hat{n}$ is the unit vector along $\mathbf{E}\times\mathbf{H}$, it appears that the refractive index in such media with $\mathrm{Re}(\varepsilon)<0$ and $\mathrm{Re}(\mu)<0$ is also negative. Such materials permit propagating waves with a reversed phase vector (**k**) compared with media with only one of Re(ε) or Re(μ) negative which do not allow any propagating modes (all waves decay evanescently in such media from the point of injection as

$k^2 < 0$). Note that in the case of the NRMs (negative refractive index materials), the Poynting vector (**S** = **E**×**H**, representing the energy flux (W/m^2) of an electromagnetic field) and the phase vector, **k**, are anti-parallel. In figure 1-1, we show the four quadrants in the Re(ε)–Re(μ) plane into which we can conveniently classify electromagnetic materials. The behavior of the waves in each of the quadrants is qualitatively different: materials that fall in the first quadrant allow the usual right-handed electromagnetic propagating waves; the materials that fall in the second and fourth quadrants do not allow any propagating waves inside them (all electromagnetic radiation is evanescently damped in these media); and the NRMs that fall in the third quadrant allow left-handed propagating waves inside them.

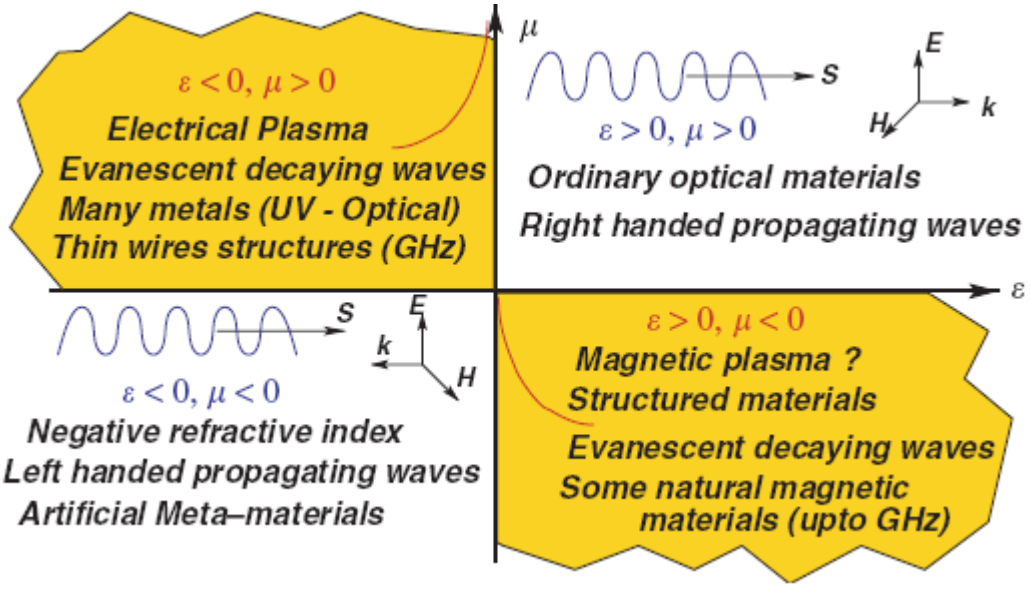

Figure 1-1. A schematic presentation of the materials classification based on the dielectric and magnetic properties. The wavy lines represent materials that allow propagating waves, and the axes set in quadrants 1 and 3 show the right- and left-handed nature of **E**, **H** and **k** vectors. The waves in quadrants 2 and 4 are decay evanescently inside the materials, which is depicted schematically. **S** is the Poynting vector. The figure is imaged from [8].

1.2 Structure of meta-materials and effects of negative permittivity (ε) and permeability (μ)

1.2.1 Negative permittivity ε

The structures depicted the effect of negative permittivity are wire-mesh structures as a negative dielectric. Pendry et al [2, 9] and Sievenpiper et al [10] independently demonstrated that metallic wire-mesh structures have a low frequency stop band from zero frequency up to a cutoff frequency, which they attributed to the motion of electrons along the metal wires. The meta-materials that Pendry et al reported consisted of very thin wires. They were structured on truly sub-wavelength length-scales, and could be effectively homogenized. The low frequency stop band was attributed to an effective negative dielectric permittivity, and provided us with a way of obtaining negative dielectrics at even microwave frequencies.

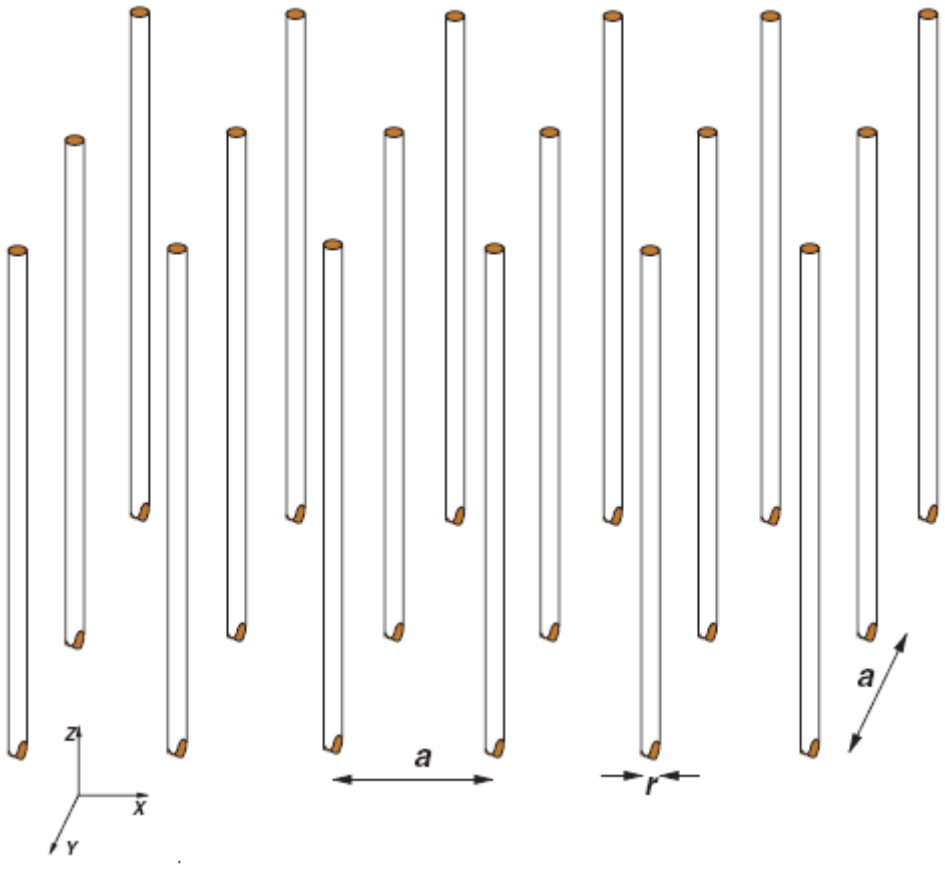

Figure 1-2. An array of infinitely long thin metal wires of radius *r* and lattice period of *a behaves* as low frequency plasma for the electric field oriented along the wires and E.M. wave oriented normal to the wires. The figure is imaged from [8].

The plasma frequency of Pendry's wire array is given by

$$f_p = \frac{c}{a\sqrt{2\pi \ln(\frac{a}{r})}} \quad \textbf{(1.3)}$$

where a is the wire lattice spacing, r is the wire radius, and c is the velocity of light. The permittivity value is given by

$$\varepsilon = 1 - \frac{\omega_p^2}{\omega(\omega + i(\varepsilon_0 a^2 \omega_p^2 / \pi r^2 \sigma))} \quad \textbf{(1.4)}$$

σ is the conductivity of metal and $\omega_p = 2\pi f_p$. In above discussion, only wires pointing in the z-direction were considered. This makes the medium anisotropic with negative ε only for waves with the electric field along the z direction and incident light normal to z-axis.

1.2.2 Negative permeability μ

The magnetic activity in most materials tends to tail off at high frequencies of even a few giga-hertz. So it was indeed a challenge to obtain magnetism, let alone negative magnetic permeability, at microwave frequencies and beyond. In the case of nano-metallic structures, the magnetic moments of induced real and displacement current distributions could actually contribute to an effective magnetization if the electric polarizability of the corresponding medium was small.

1.2.2.1 The split ring resonator (SRR)

Consider an array of concentric cylindrical metallic shells with a gap in them as shown in Figure 1-3**.** This has become well known subsequently as the split ring resonator—SRR.

The SRRs are the basis of most of the meta-materials exhibiting negative magnetic permeability nowadays [4, 5, 10–15]. The SRR works on the principle that the magnetic field of the electromagnetic radiation can drive a resonant L–C circuit through the inductance, and it therefore results in a dispersive effective magnetic permeability. The induced currents flow in the directions indicated in figure 1-3, with charges accumulating at the gaps of the rings.

The larger gap in each ring prevents the current from flowing around a single ring, but the circuit is completed across the smaller capacitive gap between two rings. Assuming that the gap (d) is rather small compared with the radius (r) and the capacitance due to the larger gaps in any single ring is negligible, we balance the emf around the circuit as

$$-i\omega\mu_0\pi r^2(H_0+j-\frac{\pi r^2}{a^2}j)=2\pi r\rho j-\frac{j}{i\omega C} \quad \textbf{(1.5)}$$

where a is the lattice constant, c is the effective capacitance , and ε is the relative dielectric permittivity of the material in the gap. It is assumed that the potential varies linearly with the azimuth angle around the ring. Proceeding as before, we obtain the effective permeability as

$$\mu_{eff}=1-\frac{\pi r^2/a^2}{1-(3d/\mu_0\varepsilon_0\varepsilon\pi^2\omega^2r^3)+i(2\rho/\mu_0\omega r)}=1+\frac{f\omega^2}{\omega_0^2-\omega^2-i\Gamma\omega}, \quad \textbf{(1.6)}$$

and thus we have a resonant form of the permittivity with a resonant frequency of

$$\omega_0=(\frac{3d}{\mu_0\varepsilon_0\varepsilon\pi^2r^3})^{1/2} \quad \textbf{(1.7)}$$

that arises from the L–C resonance of the system. The factor $f = \pi r^2/a^2$ is the filling fraction of the material. For frequencies larger than ω_0, the response is out of phase with the driving magnetic field and μ_{eff} is negative up to the 'magnetic plasma' frequency of

$$\omega_m=(\frac{3d}{(1-f)\mu_0\varepsilon_0\varepsilon\pi^2r^3})^{1/2} \quad \textbf{(1.8)}$$

assuming the resistivity of the material is negligible. It is seen that the filling fraction plays a fundamental role in the bandwidth over which $\mu < 0$. The dielectric permittivity of the embedding medium, ε, can be used to tune the resonant frequency. A finite resistivity, in general, broadens the peak, and in the case of very resistive materials the resonance is so highly damped that the region of negative μ can disappear altogether as shown in Figure1-4**.** The resonance frequency and the negative μ band can be varied by changing the inductance (area) of the loop and the capacitance (the gap width, d, or the dielectric permittivity, ε, of the material in the capacitive gap) of the system. For typical sizes of r = 1.5 mm, a = 5 mm, d = 0.2 mm, we have a resonance frequency of ω_0 = 6.41 GHz, and a 'magnetic plasma

frequency' ω_m = 7.56 GHz. The dispersion in μ_{eff} is shown in Figure1-4. We note that $\mu_{eff} \cong 1 - \pi r^2/a^2$ was changing asymptotically at large frequencies. This was due to the assumption of a perfect conductor in our analyses. One also notes that μ_{eff} can attain very large values on the low frequency side of the resonance. Thus, the effective medium of SRR is going to have a very large surface impedance $Z = \sqrt{\mu_{eff} / \varepsilon_{eff}}$.

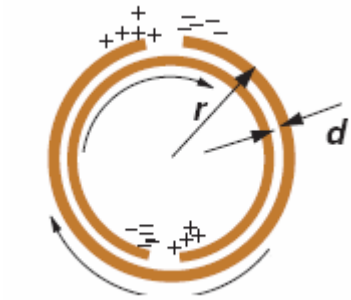

Figure 1-3. The split ring resonator (SRR) : The capacitance across the rings now causes the structure to be resonant, and split width=d, radius=r. The figure is imaged from [8].

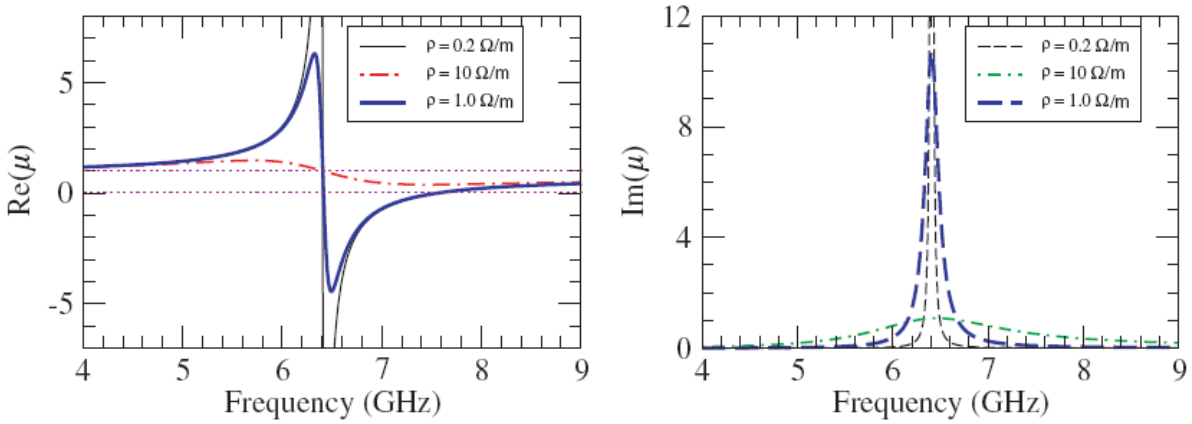

Figure 1-4. The behavior of (a) the real and (b) the imaginary parts of the effective magnetic permeability for a system of split cylinders with r = 1.5 mm, d = 0.2mm and the magnetic field along the axis for different values of ρ. The system has negative magnetic permeability for 6.41 < ω < 7.56 GHz. As the resistance increases, the response of the system tends to tail off. The figure is imaged from [8].

1.2.2.2 The Swiss roll structure at radio-frequencies

For lower radio-frequencies, the capacitance of the system can be made large instead of increasing the size of the loop (inductance), as which is a convenient way and increases the validity of our assumption of an effective medium as well. Practically, it can be achieved by rolling up a metal sheet in the form of a cylinder with each coil separated by an insulator of thickness d as illustrated in Figure1-5. This structure has also been popularly called the Swiss

roll structure. The current loop is now completed through the differential capacitance across the space between the metal sheets as shown. As before, the effective magnetic permeability for a system of such structures can be calculated as

$$\mu_{eff} = 1 - \frac{\pi r^2/a^2}{1-(dc^2/2\pi^2 r^3(N-1)\omega^2)+i(2\rho/\mu_0 \omega r(N-1))} \quad \textbf{(1.9)}$$

where N is the number of coils in the structure, and it is assumed that the total thickness of the wound layers Nd $\ll$ r the cylinder radius. This system also has the same generic resonance form of the permeability with frequency as the SRR structures, but now the resonance occurs at a much smaller frequency owing to the larger capacitance of the structure. This has seen applications in magnetic resonance imaging (MRI) at radio-frequencies as magnetic flux tubes in the region where the effective magnetic permeability assumes very large values on the lower frequency side of the resonance [16-17].

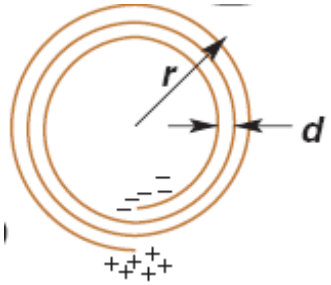

Figure 1-5. The Swiss roll structure: more capacitance for lower frequency operation. The figure is imaged from [8].

1.2.2.3 Other geometry for negative permeability

Fundamentally, the basic structures of negative permeability are composite of spilt ring with single or double rings. The main ingredients of a resonant magnetic medium are just a capacitance and an inductance. In fact, SRR structures with (1) a single ring and a single split [18–20] and (2) a double ring with a single split in each ring [21] have been proposed as candidates for a resonant magnetic medium. The point is that we would like to have an electrical polarizability as low as possible. With a single split ring, a large electric dipole moment would be generated across the capacitive gap (see Figure 1-6(a)), which could then dominate over the weaker magnetic dipole moment generated in the ring. When there are two

splits present, the dipole moments across opposite ends cancel each other. Therefore, one only gets a weak electric quadrupole moment (see Figure 1-6(c)) whose effects would be expected to be much weaker than those of the magnetic dipole moment. Most of the magnetic media that simultaneously generate an electric dipole moment are bi-anisotropic media, i.e. the constitutive relations are

$$\mathbf{D} = \varepsilon\mathbf{E} + \alpha\mathbf{H},\ \mathbf{B} = \beta\mathbf{E} + \mu\mathbf{H}, \qquad \textbf{(1.10)}$$

where α and β are the bi-anisotropy coefficients. The Ω–shaped particles first introduced as the components of a bi-anisotropic medium [22], when arranged in a periodic lattice also have a resonant ε and μ and can behave as negative magnetic materials [23]. Even the original SRR medium [3] is bi-anisotropic [24] as there is an electric dipole moment that develops across the capacitive gaps (see figure 1-6(b)), and this can also be driven by an electric field [25]. Thus the SRR is oriented such that the magnetic field is normal to the plane of the SRR and the electric field is along the SRR and can be driven by the electric field and the magnetic and electric resonances can overlap. This can be effectively resolved, of course, by rotating adjacent SRRs in the plane by 180° and the corresponding electric dipole moments would cancel. The symmetry of the single ring with two symmetrically placed capacitive gaps renders this less bi-anisotropic and electrically less active.

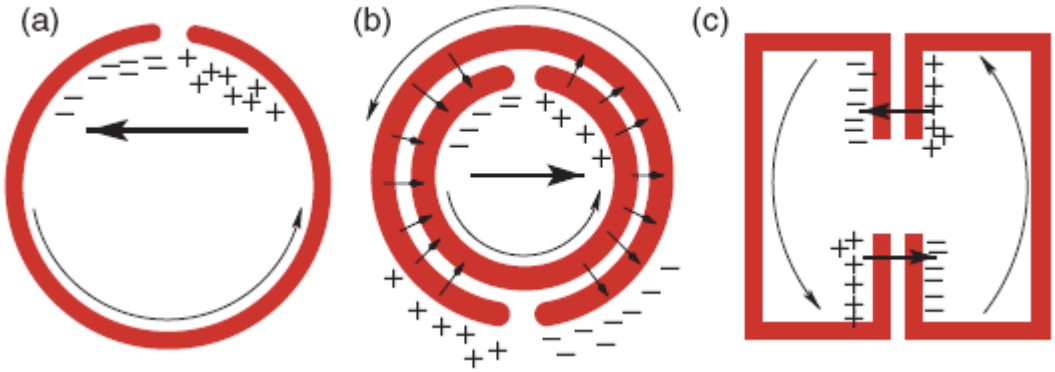

Figure 1-6. The SRRs develop an electric polarization too, although driven by a magnetic field. This bi-anisotropic behavior is maximal for (a) a single split ring which develops a large dipole moment. (b) The original SRR with two splits is also bi-anisotropic as it develops an electric dipole. The field lines due to the charges are also shown by thin lines. (c) The single ring with two symmetric splits only develops a quadrupole moment and is hardly bi-anisotropic. The figure is imaged from [8].

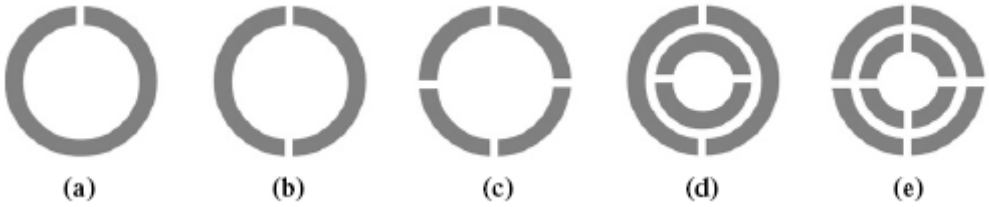

Figure 1-7. Schematic drawings of different resonator structures: (a) single ring with one cut, (b) single ring with two cuts, (c) single ring with four cuts, (d) SRR with two cuts and (e) SRR with four cuts. Figure is imaged from [26].

People then studied how splits in ring affect resonance [26], as which was driven by the need for new resonator designs for the following reasons. First of all, a conventional SRR structure is not easy to fabricate for operation at higher frequencies. As the structure is scaled down, the dimensions of the narrow split and gap regions will be very small, which may eventually lead to contact problems between the metallic regions. Conventional SRR structures were fabricated for operation at a few THz [27], but for the resonator structure working at 100 THz [28] a single ring with a single split was chosen for easier fabrication. The second reason is that SRR structures are electrically resonant for different polarizations and propagation directions [29]. This effect would suppress the LH-behavior for 3D-constructed LHMs, where EM waves would be incident on the structure from all directions. Therefore, additional splits should be added to destroy the electrical coupling effect to the magnetic resonance.

As seen from the figure, all structures show resonant behavior at certain frequencies.

Simulation results are provided in Figure 1-8(b) and experimental results were compared with the simulations. The resonance frequency of one-cut ring was measured was at 4.58 GHz, whereas numerical simulations predicted it to be 4.67 GHz. For two-cut and four-cut ring resonators, measured and simulated resonance frequencies were 7.82 and 7.5 GHz; and 12.9 and 13.1 GHz, respectively. We then varied the split width of these single-ring resonators. Figure 1-9 shows the measured resonance frequencies as a function of split width. In all cases, the magnetic resonance frequency increases with increasing split width. But the rate of changing ω_m for the one-cut ring resonator (Figure 1-9(a)), two cut ring resonator (Figure 1-9(b)), and four-cut ring resonator (Figure 1-9(c)) are different. The rate of increase is larger for structures with more splits. Since the capacitance due to all splits will change, the change in total capacitance will be larger for structures having more splits. Note that the magnetic resonance frequencies increased drastically when more cuts were introduced into the system. When the second split was placed on the ring (Figure 1-7(b)), the capacitances were connected in series. Therefore, the total capacitance was decreased approximately by a factor of 2. Because of this great amount of decrease in capacitance of individual ring resonators, the change in ω_m was much larger compared to the changes owning to split widths, gap distances and metal widths.

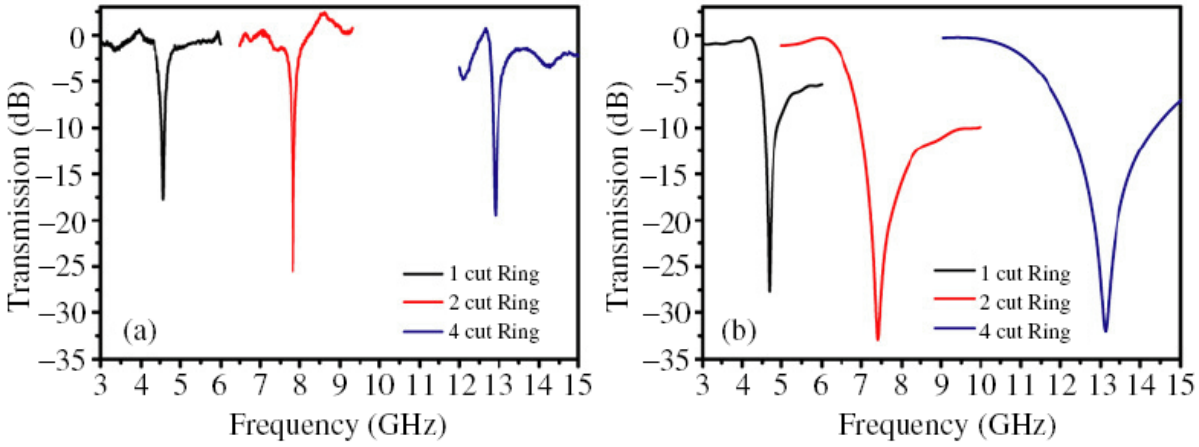

Figure 1-8. Transmission spectra of single-ring resonator with different number of cuts are shown by (a) experiments and (b) simulations. The figure is imaged from [26].

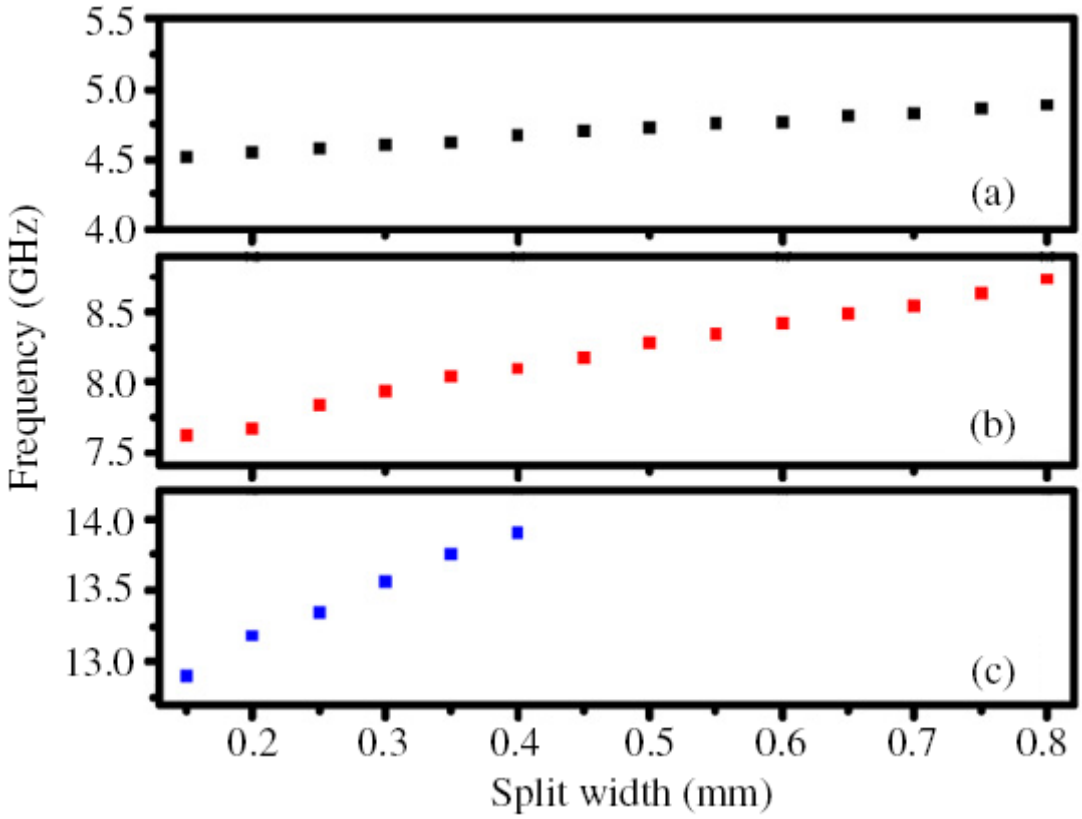

Figure 1-9. Variation of magnetic resonance frequency with the split width of (a) the one-cut ring resonator, (b) two-cut ring resonator and (c) four-cut ring resonator. The figure is imaged from [26].

For double rings with two or four cuts (splits) in each ring, as a convention, these resonator structures are called two-cut SRR (Figure 1-7(d)) or four-cut SRR (Figure 1-7(e)), where the number of cuts presented the number of splits in each ring. The split width was initially taken with a size of d=0.2 mm. Measured and simulated transmission spectra of these structures are depicted in Figure 1-10(a) and 1-10(b), respectively. The resonance frequency of the one-cut SRR was found at 3.63 and 3.60 GHz, from both measurements and

simulations. For two-cut SRR and four-cut SRR structures, measured and simulated resonance frequencies were 6.86 and 6.45 GHz, and 12.96 and 13.2 GHz, respectively. We then varied the split width of all splits in both inner and outer rings. Figure 1-11 shows the measured resonance frequencies as a function of split width. In all cases the magnetic resonance frequency increased with increase of split width. Similar to the behavior observed in single split ring, the rate of increase in resonance frequency was also larger for structures having more splits.

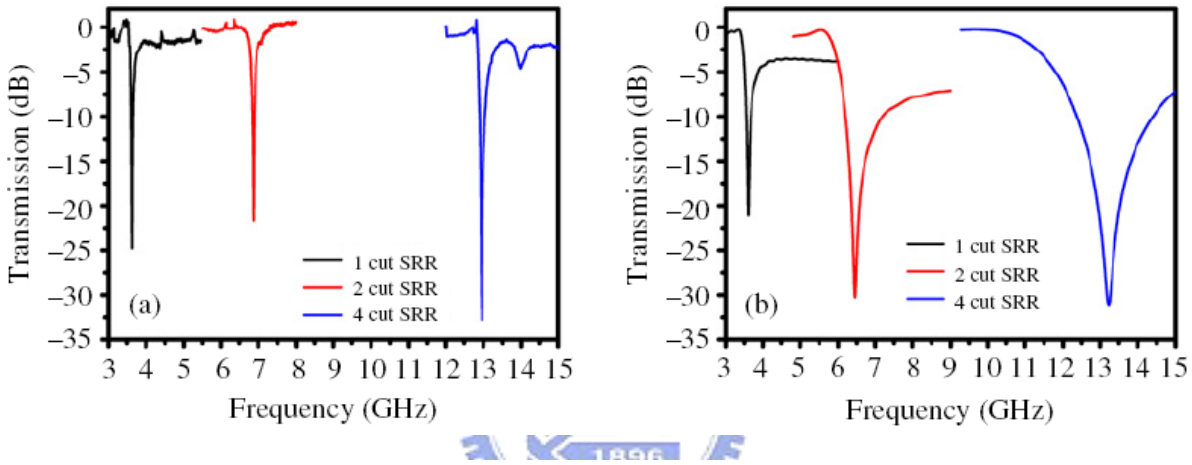

Figure 1-10. Transmission spectra of SRRs with different number of cuts obtained from (a) experiments and (b) simulations. The figure is imaged from [26].

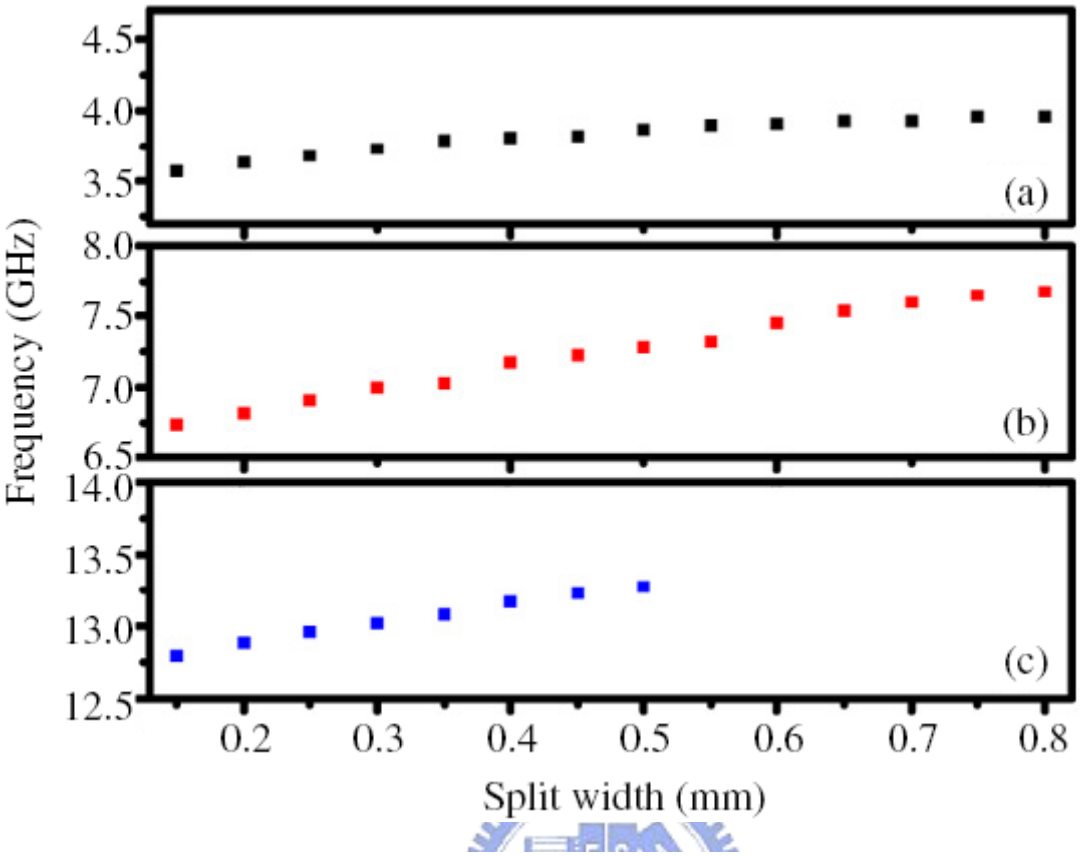

Figure 1-11. Variation of magnetic resonance frequency with the split width of (a) the one-cut SRR, (b) two-cut SRR and (c) four-cut SRR. The figure is imaged from [26].

Table 1-1 summarizes the measured resonant frequencies obtained for six different split ring resonator structures for some detailed analyses and a comparison of the results obtained in single split rings and double split rings. Columns represent the number of rings in the resonator structures, whereas the rows correspond to the number of cuts in each ring. Increasing the number of splits increases the magnetic resonance frequency drastically, since the amount of decrease in the capacitance of the system is very large. For one-cut and two-cut resonator structures, the amount of decrease of ω_m is around 1 GHz. But in the case of the four-cut structure, such a behavior is not observed. There is essentially no change in resonant frequency between both configurations. The orientation of the splits is important in this case. Unlike the anti-symmetric orientations of splits in the one-cut and two-cut SRRs, the four-cut SRRs have symmetric orientations. So the mutual capacitance between the inner and outer rings is very small. This is due to the fact that the induced charges along both the rings have

the same sign and a similar magnitude. As a result, addition of a second ring does not affect the overall capacitance of four-cut single-ring resonator. In turn, the resonance frequency did not change appreciably.

	Single-ring resonator	Double-ring resonator
One cut	4.58 GHz	3.63 GHz
Two cut	7.82 GHz	6.86 GHz
Four cut	12.9 GHz	12.96 GHz

Table 1-1. Measured magnetic resonance frequencies for six different resonator structures. The figure is imaged from [26].

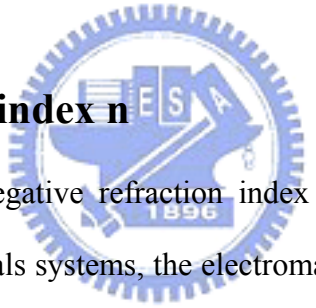

1.2.3 Negative refraction index n

There is no material with negative refraction index in nature. However, with some design of structures in some materials systems, the electromagnetic wave at certain frequency range could propagate a medium with $\mathrm{Re}(\varepsilon) < 0$ and $\mathrm{Re}(\mu) < 0$ simultaneously, such that a negative refractive index value is expected to be observed in these artificial materials. .

1.2.3.1 Composite meta-materials (CMM = SRR+WIRE)

Smith et al [4] proposed a composite, which was constructed by combination of the thin wire medium with $\varepsilon < 0$, and the SRR medium with $\mu < 0$, would yield an effective medium with $n < 0$. Such materials are called meta-materials.

The calculations and experimental measurements [4, 30] showed this was a realistic way to observe negative refractive index. Two compositing ways of this type meta-material were reported. One of them [31] was constructed by alternatively stacking the SRR and wire mediums in a periodic manner as shown in Fig. 1-12(d) (material was copper). The

periodicity along direction was 6.5 mm, the same as in SRR and wire mediums. The measured transmission and reflection properties of the composite meta-material are displayed in Fig. 1-15. There appeared a broad pass-band extending from 9.6 to 14.3 GHz. The average transmission within the pass-band was around 4.5dB, corresponding to a transmission 0.3 dB for each unit cell. This transmission was significantly higher than the previously reported composite meta-material transmission properties [32-34]. As can be seen from Figures. 1-13 and 1-14, in this frequency range, the values of both effective permeability and permittivity were negative. It deserves to point out that if only one of the constitutive parameters is negative and the other is positive one would observe evanescent waves rather than propagating waves in the medium. So, the structure can be named as a DNG meta-material [35]. The reflection of the double-negative structure within this frequency range was quite low. This indicated that most of the EM waves penetrated into the DNG composite medium, and there was a certain amount of scattering loss at these frequencies [36-37]. The reflection of the structure is around unity for the first stop-band region, which suggests that the composite structure acted as an almost perfect mirror for these frequencies.

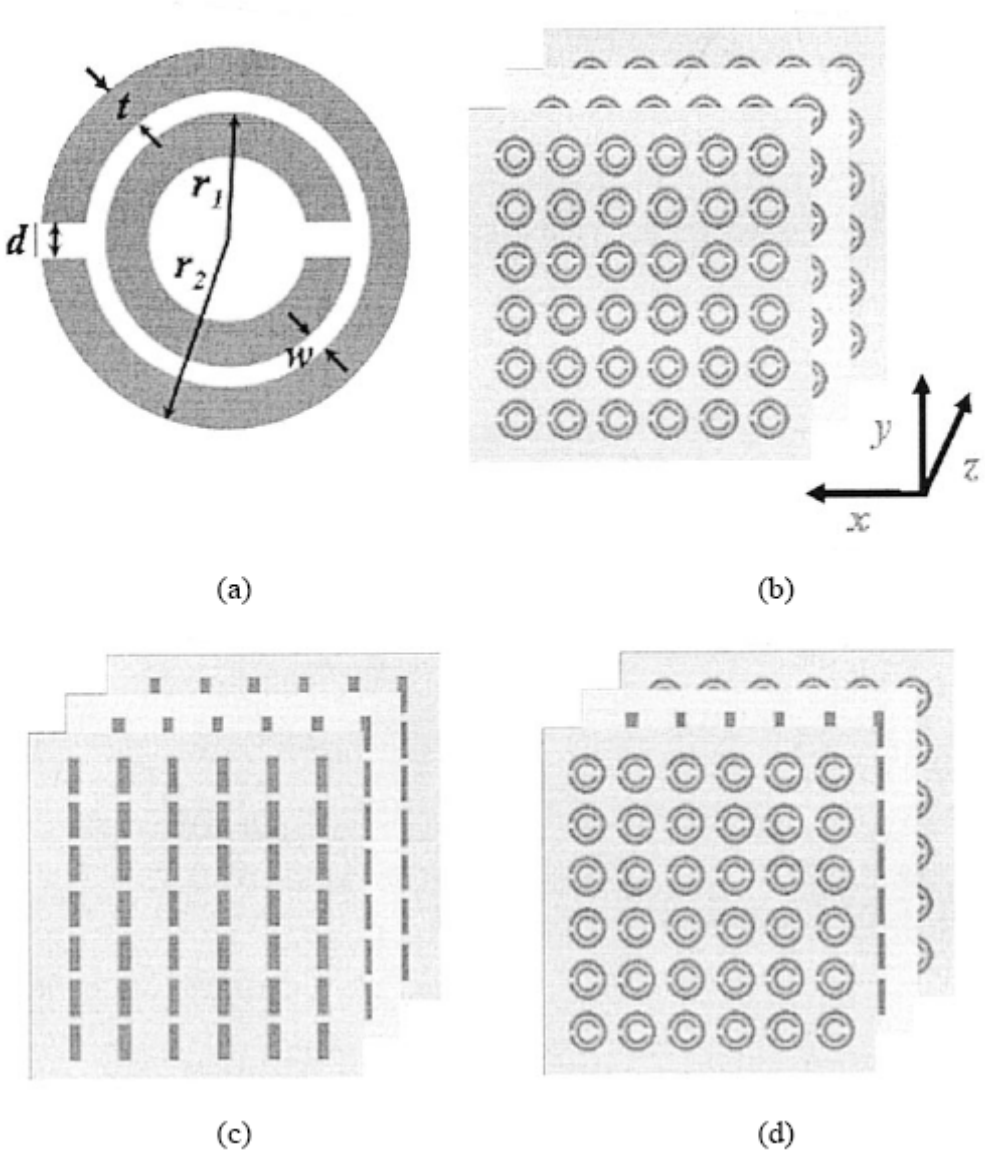

Figure 1-12. (a) A single copper SRR with parameters r_1 = 2.5 mm, r_2 = 3.6 mm, d = w = 0.2 mm, and t = 0.9 mm. Schematic drawing of (b) the negative μ medium, (c) the negative ε medium, and (d) the composite DNG(double negative) meta-material. The figure is imaged from [31].

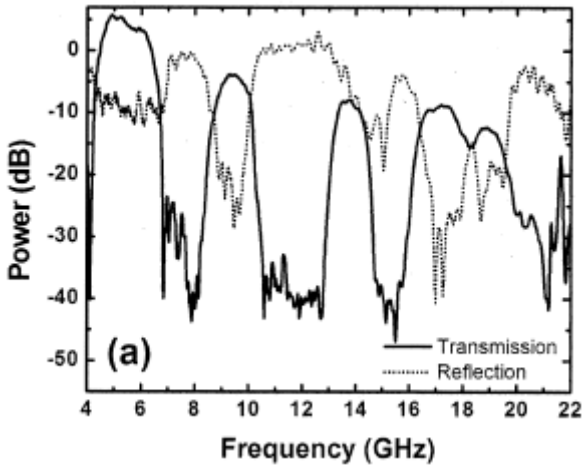

Figure 1-13. Measured broad-range transmission and reflection spectra of the SRR medium along x direction in free space. The transmission spectrum exhibits series stop-bands and pass-bands. The negative permeability regions do not allow the propagation of electromagnetic waves through the SRR structure. The figure is imaged from [31].

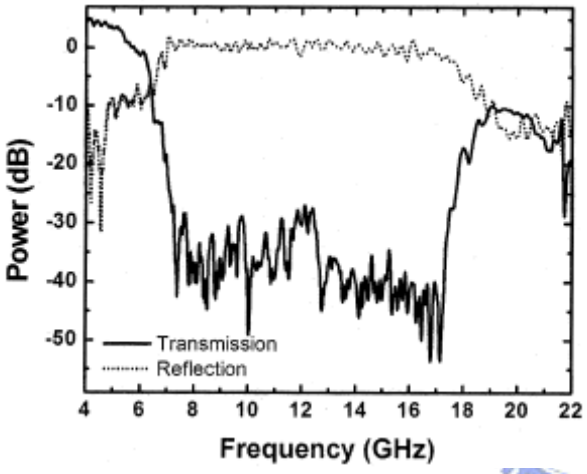

Figure 1-14. Measured transmission and reflection characteristics of the thin wire medium. The transmission spectrum exhibits a wide stop-band extending from 7 to 18 GHz. The lower pass-band is observed due to discontinuous nature of the wires. The reflection data also indicates the strong rejection of electromagnetic waves from the crystal for the negative permittivity region. The figure is imaged from [31].

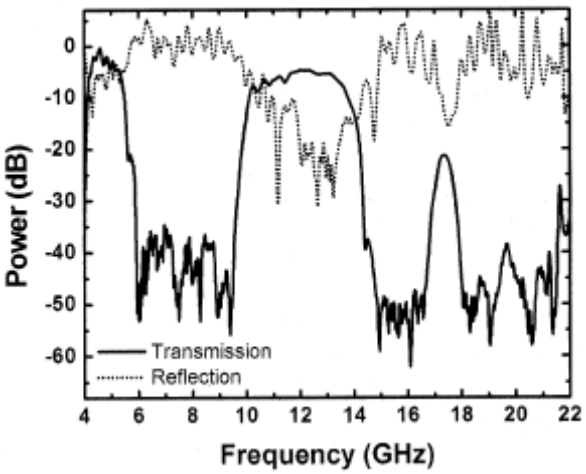

Figure 1-15. Measured transmission and reflection spectra of the DNG composite meta-materials. Relatively high power, -4.5 dB, is measured between frequencies 9.5 and 14.5 GHz in which both effective permittivity and permeability have negative values. The reflection spectrum also has average -20 dB rejection throughout this region. The figure is imaged from [31].

Another way of forming the composite of SRR and WIRE was putting SRR and WIRE side by side [38]. Figure 1-16 shows an overview of the structures and the parameters used for calculations. Five geometric variants were considered there, involving four different radii and a fat version. The sets of geometric parameters and boundary frequencies for a rod–split-ring

(RSR) patterned material to become left-handed in the lower THz spectral range are given in Table 1-2. Numerical simulations of a plane wave impinging on the RSR composite structure were performed using the MWS (Microwave studio) code. Three angles of incidence were chosen, namely 0°, 45°, and 90°, with the magnetic field pointing along ether split-ring axes in the latter case. The electric field was polarized either parallel or perpendicular to the rods. It was confirmed that the case of 90° incidence angle to the normal and the **E** field parallel to the rods showed the signature of the meta-material most clearly. In Figure 1-17 the ratio of the amplitudes of the transmitted and incident waves, which was represented as S_{21} that was used in the MWS code, is shown for the individual cases of rods only, split ring resonators (SRR), and RSR for the Ni slim ring. The transmission of either rods or SRRs are small, indicating negative ε_{eff} and μ_{eff}, respectively, while the composite material shows a transmission peak as expected.

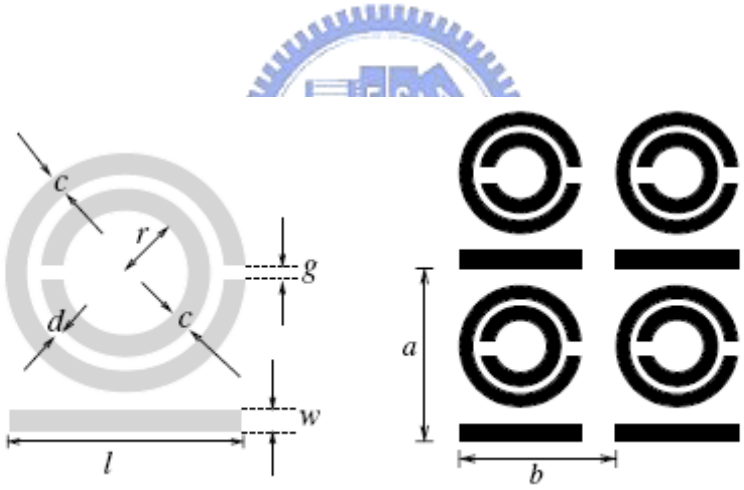

Figure 1-16. Geometric parameter definition of the RSR (left). Periodic arrangement of the RSR adopted for micro-fabrication (right). The figure is imaged from [38].

	r/μm	c/μm	d/μm	a/μm	b/μm	ν_0/THz	ν_{mp}/THz
Ni slim	10	10	10	110	90	2.63	2.68
Ni fat	10	15	10	135	110	2.63	2.67
Au 1	8.4	12	4.3	95.4	78.4	2.24	2.28
Au 2	11	12	4.3	100.6	83.6	1.50	1.53
Au 3	14	12	4.3	106.6	89.6	1.04	1.08

[a]For all structures $g = 5$ μm, $l = (r + 2c + d) \times 2$. For Ni, $w = 10$ μm while for Au, $w = 12$ μm.

TABLE 1-2. THz specifications of a rod–split-ring structure. The tale is imaged from [38].

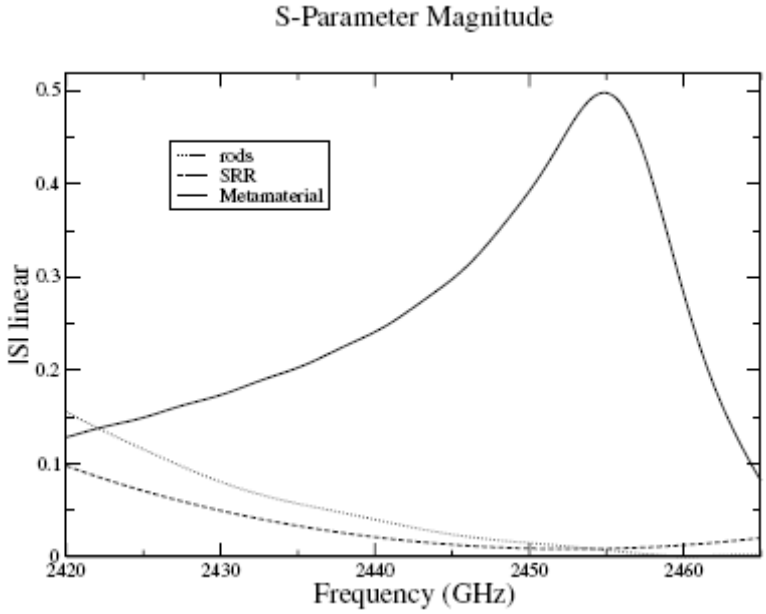

Figure 1-17. Amplitude ratio of transmitted and incident waves as expressed by the parameters S_{21} (linear scale) in MWS for the rods, SRR and RSR. The figure is imaged from [38].

Chapter 2

Materials and goal

2.1 Introduction

In this chapter, Materials that were used for fabrication of metal structures of SRR, WIRE and CMM (composite of SRR and WIRE) in the thesis work are discussed. Section2.2 deals with the process advantages why choosing copper for fabrication of meta-materials, and some optical properties of copper. Section2.3 describes the experimental goal - what was expected, and what have been observed and achieved.

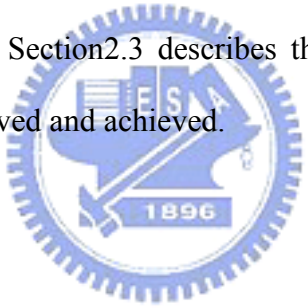

2.2 materials

2.2.1 Advantages of process

Copper metallization has nowadays been the standard technology for chip fabrication. The commonly used method of copper metallization is blanket Cu electroplating to fill in gaps and trenches of damascene structures, followed by chemical mechanical polishing (CMP) to remove the overburden of Cu and TaN barrier for flatness of the surface. To completely remove the overburden of copper and tantalum or titanium nitride barrier outside the trenches using CMP would be difficult, owing to the non-uniform removal selectivity. On the other hand, regarding the increasing aspect ratio of wires and vias, Coating of Cu seeding prior to Cu electroplating using conventional physical vapor deposition (PVD) would be limited by

step-coverage beyond 0.10 mm (what is the unit), due to poor coverage along sidewalls and at bottom corners or overhanging on the top corners. Although chemical vapor deposition (CVD) or electrode-less Cu seeding could improve the step coverage, the Cu seed formed by CVD would suffer from the carbon or nitrogen impurities decomposed from the metallic-organic precursors, and consequently rough surface.

In this experiment, the selective Cu metallization process based on electrochemical replacement reaction was employed, instead of the above mentioned conventional processing using a combination of Cu seeding, electroplating, and the complicated multi-step CMP steps. Through the implementation of the intrinsically selective Cu contact displacement from amorphous Si and the relative simple Si CMP to remove the overburden of Si outside the trenches, the selective Cu metallization was successfully carried out.

2.2.2 Optical properties of copper

Gold, silver and copper are mono-valent metals, so it can be approximated using simple "free electron model". Compared to alkali metals, these three metals are much easier to handle. Their optical properties, especially in the red and infrared wavelength range are of interest, because they are almost entirely attributed to the free electron.

According to [39], S. Roberts defined the dielectric constant as k=k'-ik". He showed a list of dielectric varieties with incident wavelengths ranged from 0.365um to~2.5um. As depicted in Table 2-1, one can see that E.M waves will collapse at this range. When increasing frequency (decreasing wavelength), both -k' and k" decrease. Since $k=\omega\sqrt{\varepsilon\mu}$, the dielectric constant increases with the amplitude decay of E.M waves rapidly. S. Roberts also pointed out that in the wavelength range below 0.6um the data confirm that there is low transmission (i.e. high absorption) due to inter-band electronic transitions. At longer wavelengths the optical properties are determined almost entirely by free electrons model.

λ	90°K		300°K		500°K	
	$-K'$	K''	$-K'$	K''	$-K'$	K''
0.365	3.35	4.36	3.14	4.44	2.01	3.88
0.405	4.15	4.77	4.08	4.93	3.12	4.42
0.436	4.98	5.10	4.91	5.27	4.06	4.67
0.50	6.68	5.78	6.69	5.74	5.77	5.32
0.55	6.51	4.40	6.76	4.30	6.22	4.06
0.578	8.06	1.20	8.26	1.88	7.48	2.28
0.60	11.08	0.65	10.78	0.98	9.60	1.38
0.65	15.52	0.62	15.28	0.84	14.00	1.00
0.75	23.95	0.78	23.85	1.01	22.38	1.32
1.0	48.19	1.48	48.05	2.04	46.10	2.68
1.5	114.3	4.03	114.0	5.69	110.4	7.51
2.0	205.7	8.75	205.2	12.38	198.4	16.29
2.5	311.0	15.53	310.8	22.02	299.6	28.83

Table 2-1. Optical properties of copper at T=90^0, 300^0, and 500^0K. The table is imaged from [39].

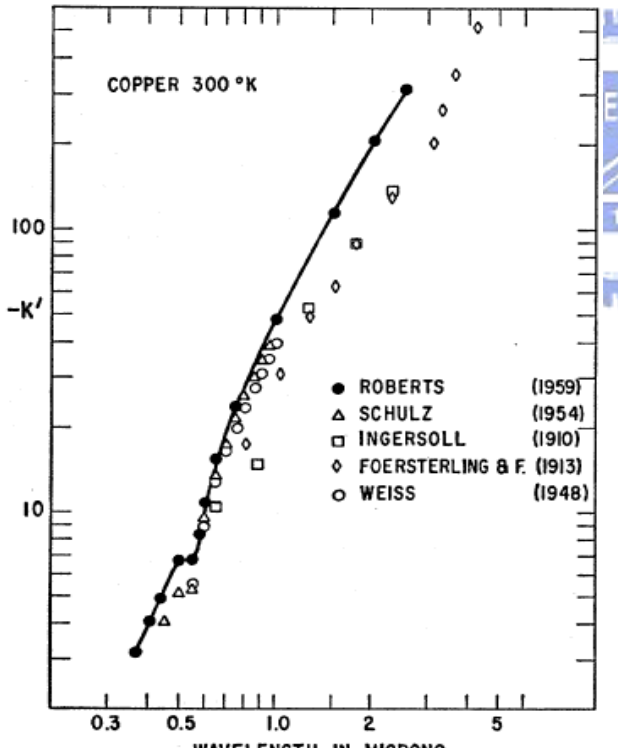

Figure 2-1. Real part of dielectric constant of copper at 300^0K. The figure is imaged from[39].

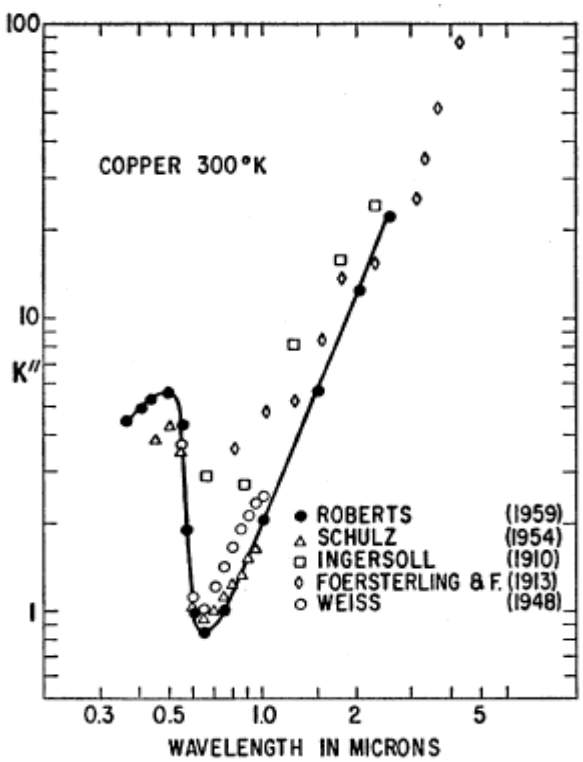

Figure 2-2. Imaginary part of dielectric constant of copper at 300^0K. The figure is imaged from[39].

2.3 Goal and a short summary of the work

Our general goal is to construct meta-materials that could have negative permittivity or

negative permeability at the multiple terahertz frequency range, namely covering from mid-infrared (IR) to near-IR and eventually visible light. Copper (Cu) has a spectra range over mid-near IR, so it is a suitable material for this purpose. A rising interest in using Cu is linked to the recent advances of Cu implementation for metal wiring in Si chip technology.

To obtain meta-materials that responding at even higher frequency, it need to reduce the geometrical size of patterns, or change to use lower damping metals, e.g., Ag and Au. It thus challenges the process technology in both lithography of linewidth and metal etching. A new fabrication technology has then been developed, in which the backbone Si patterns were first formed by trench filling using PECVD, followed by CMP. These patterns were finally converted to Cu by chemical reactions for replacement.

Three patterns, namely, SRR, WIRE, and CMM, have been designed with an expectation that have meta-materials with a negative permittivity, negative permeability, and eventually negative refractive index, respectively. The desired spectral range is to appear at mid-IR close to far-IR.

Optical measurements were performed utilizing FTIR, and it was observed different reflection spectra from the samples using the incident IR beam with different polarizations. After data processing for peak normalization and noise suppression in background, it was observed enhanced reflection peak that was introduced by artificial magnetism and electric resonance due to negative permittivity/permeability.

Simulations of the electromagnetic propagation behavior along with these patterns were made using a commercial code of Computer Simulation Technology (CST), and a comparison with our experimental results was made for all three pattern designs at various frequencies, which provided more understanding on physical nature how the negative refractive index was originated in such plamonic systems.

Chapter 3

Mechanism and properties of meta-materials

3.1 Introduction

The mechanism and properties of meta-materials are discussed in more detail in this chapter. In this thesis work, three types of patterns, i.e., SRR, WIRE, and CMM were designed, processed, and characterized. Beginning from E.M waves induce current and displacement current, the mechanism how light cannot pass through in certain frequency range is discussed. In general, Most of the magnetic media that simultaneously generate an electric dipole moment are bi-anisotropic media. Thus, an explanation how this effect was related to electric or magnetic activity in different ways to produce negative permittivity/permeability is given.

3.2 Split ring resonator (SRR)

The discussion starts with a single split ring resonator, since it is the simplest example for understanding the physical mechanisms that produce effective negative permittivity /permeability. For a single split ring resonator, when the applied magnetic field has a component normal to the plane of ring resonator, it will excite a current loop around the ring. The split structure offer an effect of capacitance, then the current excited by external magnetic field will be circulated through a serials circuit of inductance and capacitance.

It is known that resonance occurs at the frequency $\omega_m=\frac{1}{\sqrt{LC}}$, in which there is a strong absorption of the external magnetic field. This effect results in an effective permeability that is smaller than zero. The primary physical mechanism is described above, being interest us news to understand how micro or nano-structures have an influence on E.M waves.

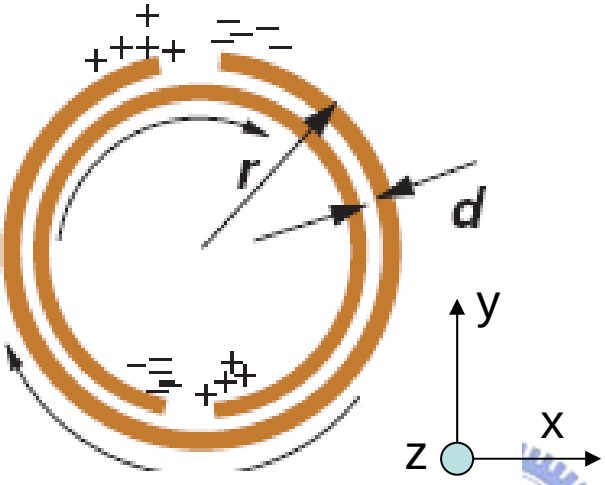

Figure 3-1. Structure of SRR. The axial magnetic field is along z-axis. The figure is imaged from [8].

Below are more quantitative discussions on physical properties of SRR. Most materials have a natural tendency to be diamagnetic as a consequence of Lenz's law. Consider the response of SRR arrays to an incident electromagnetic wave with the magnetic field normal to the plane, as shown in Figure 3-1. The SRR has a radius r, and is placed in the square lattice with a period of a. The oscillating magnetic field normal to the plane of SRR induces circumferential surface currents which tend to generate a magnetization opposing to the applied field. The axial (z-axis) magnetic field inside the cylinders is

$$\mathbf{H}=\mathbf{H_0}+\mathbf{J}-\frac{\pi r^2}{a^2}\mathbf{J} \qquad \textbf{(3.1)}$$

where $\mathbf{H}_0$ is the applied magnetic field and **J** is the induced current per unit length of the SRR. The third term $\frac{\pi r^2}{a^2}\mathbf{J}$ is due to the depolarizing field, which is assumed to be uniform as the SRR are infinitely long along the z-axis. The electromagnetic force (emf) around the SRR can be calculated according to the Lenz's law and is balanced by the Ohmic drop in potential：

$$-i\omega\mu_0\pi r^2(H_0+J-\frac{\pi r^2}{a^2}J)=2\pi r\rho J-\frac{J}{i\omega C} \quad \textbf{(3.2)}$$

where the effective capacitance $C = \varepsilon_0\varepsilon\pi r/(3d)$, and ε is the relative dielectric permittivity of the material in the gap. It is assumed that the potential varies linearly with the azimuthal angle around the ring.

The system of SRRs is homogenized by adopting an averaging procedure that consists of averaging the magnetic induction, B, over the area of the unit cell while averaging the magnetic field, H, over a line along the edge of the unit cell. The averaged magnetic field is

$$B_{eff}=\mu_0 H_0 \quad \textbf{(3.3)}$$

While the averaged H field outside the SRR is

$$H_{eff}=H_0-\frac{\pi r^2}{a^2}J \quad \textbf{(3.4)}$$

Using above equations, it is obtained the effective relative magnetic permeability：

$$\mu_{eff}=\frac{B_{eff}}{\mu_0 H_{eff}}=1-\frac{\pi r^2/a^2}{1-(3d/\mu_0\varepsilon_0\varepsilon\pi^2\omega^2 r^3)+i(2\rho/\mu_0\omega r)}=1+\frac{f\omega^2}{\omega_0^2-\omega^2-i\Gamma\omega} \quad \textbf{(3.5)}$$

and thus it derives a resonant form of the permittivity with a resonant frequency of

$$\omega_0=\sqrt{\frac{3d}{\mu_0\varepsilon_0\varepsilon\pi^2 r^3}} \quad \textbf{(3.6)}$$

that arises from the L–C resonance of the system. The factor $f = \pi r^2/a^2$ is the filling fraction of the material. For frequencies larger than ω_0, the response is out of phase with the driving magnetic field and μ_{eff} is negative up to the 'magnetic plasma' frequency of

$$\omega_m=\sqrt{\frac{3d}{(1-f)\mu_0\varepsilon_0\varepsilon\pi^2 r^3}} \quad , \quad \textbf{(3.7)}$$

assuming the resistivity of the material is negligible, and it is seen that the filling fraction plays a fundamental role in the bandwidth over which $\mu < 0$. It is noted that $\mu_{eff} = 1 - \pi r^2/a^2$ asymptotically at large frequencies. This is due to the assumption of a perfect conductor in above analyses. It deservers to be mentioned that μ_{eff} can attain very large values on the low frequency side of the resonance. Thus, the effective medium of SRR is going to have a very

large surface impedance $Z = \sqrt{\frac{\mu_{eff}}{\varepsilon_{eff}}}$.

In the following section, the electric coupling to the magnetic resonance of split ring resonators is discussed [40]. According to [40], authors observed unexpectedly that the incident electric field coupled to the magnetic resonance of the SRR, when the E.M. waves propagated perpendicular to the SRR plane while the incident E was parallel to the gap-bearing sides of the SRR.

It was recently shown [41-42] that the SRRs exhibited electric resonant response in addition to their magnetic resonant response. As a result of this electric response and its interaction with the electric response of the wires, the effective plasma frequency, ω_p', was much lower than the plasma frequency of the wires, ω_p. An easy criterion [41] to identify whether an experimental transmission peak was left-handed (LH) or right-handed (RH) was proposed, i.e., If closing the gaps of the SRRs in a designed LH structure would remove only one single peak from the transmission data in the low frequency regime, it could be a strong evidence to assign that transmission peak due to the LH effect. The authors reported numerical and experimental results for the transmission coefficient of a lattice of SRRs alone for different orientations of the SRR with respect to the external electric field, **E**, and the direction of propagation. It was considered an obvious fact that an incident EM wave excited the magnetic resonance of the SRR only through its magnetic field; hence one could conclude that this magnetic resonance appeared only if the external magnetic field **H** was perpendicular to the SRR plane, which in turn implied a direction of propagation parallel to the SRR [Figures. 3-2(a), and 1(b)]. If **H** was parallel to the SRR [Figures. 3-2(c), and 1(d)] no coupling to the magnetic resonance was expected. However, the present work shows that this was not always the case. If the direction of propagation was perpendicular to the SRR plane and the incident **E** was parallel to the gap-bearing sides of the SRR [Figure 3-2(d)], an electric

coupling of the incident EM wave to the magnetic resonance of the SRR occurred. It thus means that the electric field excited the resonant oscillation of the circular current inside the SRR, influencing the behavior of either only ε(ω) [in Figure 3-2(d)] or both ε(ω) and μ(ω) [in Figure 3-2(b)].

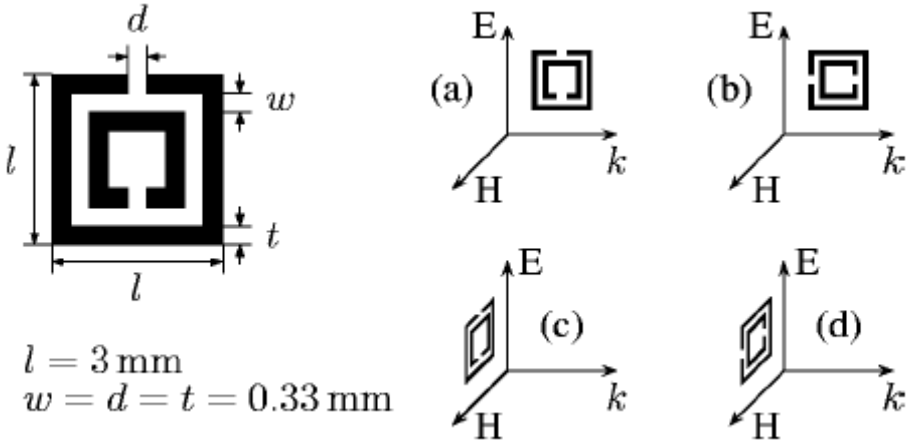

Figure 3-2. Left–hand side: SRR geometry studied. Right–hand side: The four studied orientations of the SRR with respect to the triad **k**, **E**, **H** of the incident EM field. The two additional orientations, where the SRR are on the **H-k** plane, produce no electric or magnetic response. The figure is imaged from [40].

Four nontrivial orientations of the SRR are considered, as shown in Figure 3-2, while the measured transmission spectra, T, of the composite meta-material (CMM) are presented in Figure.3-3. The continuous line (line a) corresponds to the conventional case (Figure 3-2(a)), with **H** perpendicular to the SRR plane and **E** parallel to the symmetry axis of the SRR. Notice that T exhibited a stop band at 8.5–10.0 GHz, due to the magnetic resonance. The dashed line (line b) shows T for the orientation of Fig. 3-2(b); here **E** was no longer parallel to the symmetry axis of the SRR and thus there was no longer a mirror symmetry of the combined system of SRR plus EM field. Notice that now T exhibited a much wider stop band at 8–10.5 GHz, starting at lower frequency. An interesting result was obtained by comparing T for the two cases shown in Figures. 3-2(c) and 3-2(d), for which there was no coupling to the magnetic field since **H** was parallel to the SRR plane. For the case of Figure 3-2(c), where

E was parallel to the symmetry axis, no feature was observed around the magnetic resonance frequency (line c) in Figure 3-3, as expected. However in the case of Figure 3-2(d), where the SRR plus EM field exhibited no mirror symmetry, a strong stop band in T around ω_m was observed (line d), similar to that of the conventional case [Figure 3-2(a)]. It thereby strongly suggested that the magnetic resonance could be excited by the electric field if there was no mirror symmetry.

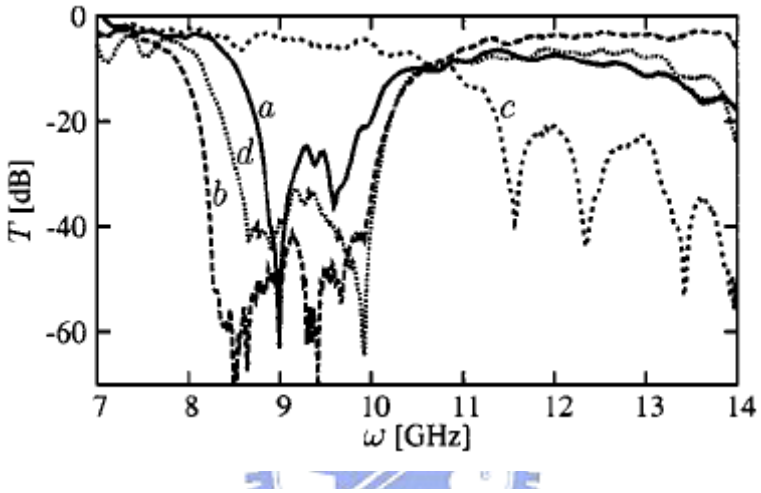

Figure 3-3. Measured transmission spectra of a lattice of SRRs for the four different orientations shown in Figure 3-2. The figure is imaged from [40].

At low frequencies, the SRR can basically be only represented by its outer ring. As shown in Figure 3-4, the SRR ring will experience different spatial distributions of the induced polarization, depending on the relative orientation of **E** with the SRR gap. If **E** is parallel to the no gap sides of the SRR, its polarization will be symmetric and the polarization current is only flowing up and down the sides of the SRR, as shown in Figure 3-4(a). If the SRR is turned by 90°, as shown in Fig. 3-4(b), the broken symmetry leads to a different configuration of surface charges on both sides of the SRR, connected with a compensating current flowing between the sides. This current contributes to the circulating current inside the SRR and hence couples to the magnetic resonance.

This unexpected electric coupling to the magnetic resonance of the SRR is of

fundamental importance in understanding the refraction properties of SRRs in the low frequency region of the EM spectrum.

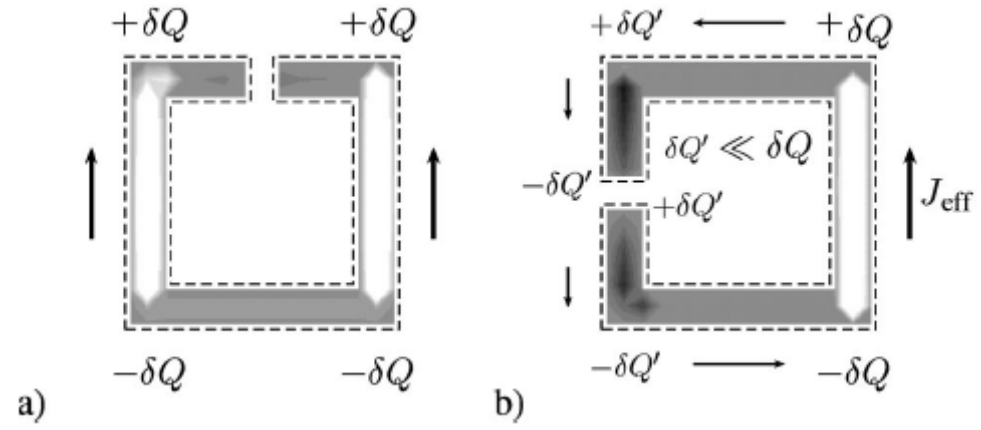

Figure 3-4. Schematic drawing for the polarization in two different orientations of a single ring SRR. The external electric field points upward. Only in case of broken symmetry (b) a circular current will appear which excites the magnetic resonance of the SRR. The interior of the ring shows FDTD data for the polarization current component $J_{\|E}$ at a fixed time for normal incidence [Figures 3-2(c) and 3-2(d)] as a gray scale plot. The figure is imaged from [40].

3.3 Wire-mesh structure as negative dielectric (WIRE)

Consider an array of infinitely long, parallel and very thin metallic wires of radius r placed periodically at a distance a in a square lattice with $a \gg r$ as shown in Figure 3-5. The electric field is considered to be applied parallel to the wires (along the Z axis). The electrons are localized to move only within the wires, as which has the first effect of reducing the effective electron density since the radiation cannot sense the individual wire structure but only the average charge density. The effective electron density is immediately represented by

$$n_{eff} = \frac{\pi r^2}{a^2} n \qquad \textbf{(3.8)}$$

where n is the actual density of conduction electrons in the metal.

There is a second equally important effect to consider. The thin wires have a large inductance, and it is not easy to change the currents flowing in these wires. Thus, it appears as

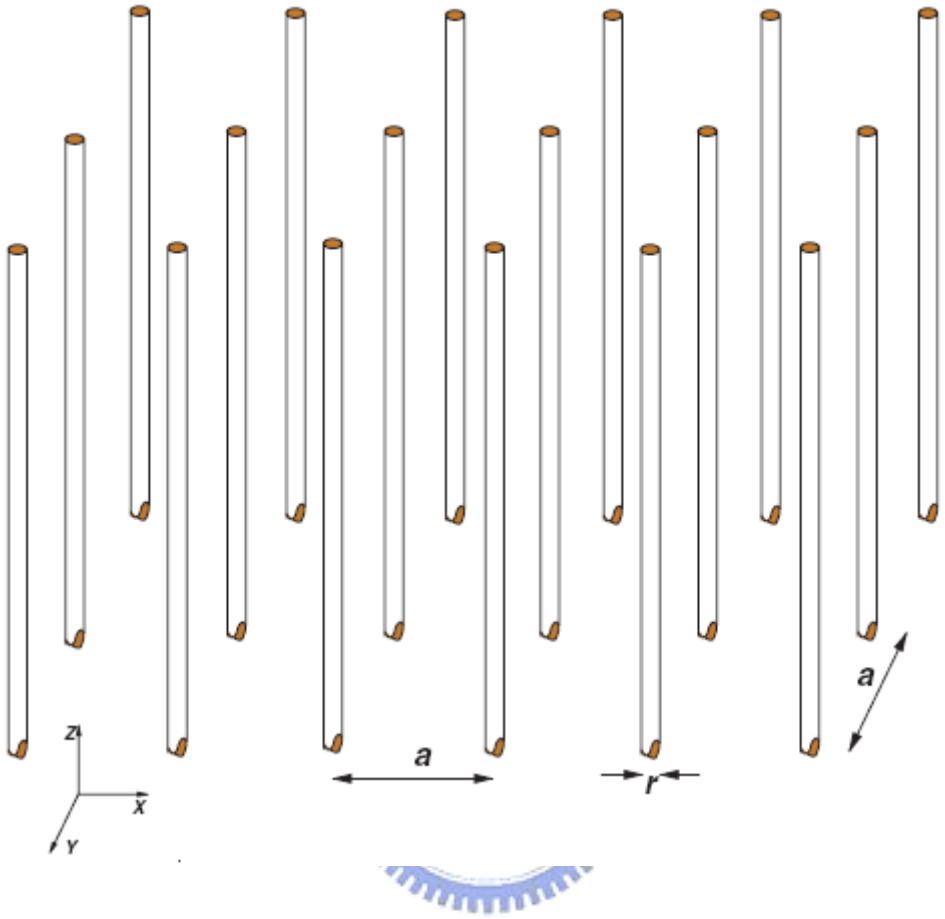

Figure 3-5. An array of infinitely long thin metal wires of radius r, and a lattice period of behaves as a low frequency plasma for the electric field oriented along the wires and E.M. wave oriented normal to the wires. the figure is imaged from [8].

if the charge carriers, namely the electrons, have acquired a tremendously large mass. By symmetry there is a point of zero field between the wires, and hence the magnetic field along the line between two wires can be estimated by

$$\mathbf{H}(\rho)= \frac{\hat{\varphi} I}{2\pi}\left(\frac{1}{\rho}-\frac{1}{a-\rho}\right) \qquad \textbf{(3.9)}$$

The vector potential associated with the field of a single infinitely long current-carrying conductor is non-unique, unless the boundary conditions are specified at definite points. In our case, there is a periodic medium that sets a critical length of a/2. The vector potential

associated with a single wire can thus be approximated by

$$\mathbf{A}(\rho)= \frac{\mu_0 \hat{z} I}{2\pi} \ln[\frac{a^2}{4\rho(a-\rho)}] \qquad \forall \rho < \frac{a}{2} \qquad \textbf{(3.10)}$$

$$\mathbf{A}(\rho)=0 \qquad \forall \rho > \frac{a}{2} \qquad \textbf{(3.11)}$$

This choice avoids the vector potential of one wire overlapping with another one, and thus the mutual induction between any two adjacent wires is addressed to some extent. Noting that $r \ll a$ by about three orders of magnitude in the present model, and the current $I = \pi r^2 nev$, where v is the mean electron velocity, the vector potential can be written as

$$\mathbf{A}(\rho)= \frac{\mu_0 r^2 nev}{2} \ln[\frac{a}{\rho}]\hat{z} \qquad \textbf{(3.12)}$$

This is a very good approximation in the mean field limit, when considering only two wires, but in fact the lattice has actually a four-fold symmetry. The actual deviations from this expression are much smaller than in this case. It is noted that the canonical momentum of an electron in an electromagnetic field is $\mathbf{p} + e\mathbf{A}$. Thus assuming that the electrons flow on the surface of the wire (assuming a perfect conductor), one can express the momentum per unit length of the wire as

$$\mathbf{P}= \pi r^2 ne A(r) = \frac{\mu_0 \pi r^4 n^2 e^2 v}{2} \ln(\frac{a}{r}) = m_{eff} \pi r^2 nv \qquad \textbf{(3.13)}$$

in which $m_{eff\ is}$ an effective mass

$$m_{eff}= \frac{\mu_0 r^2 ne^2}{2} \ln(\frac{a}{r}) \qquad \textbf{(3.14)}$$

for the electron.

Thus, assuming a longitudinal plasmonic mode for the system, one derives

$$\omega_p^2 = \frac{n_{eff} e^2}{\varepsilon_0 m_{eff}} = \frac{2\pi c^2}{a^2 \ln(a/r)} \qquad \textbf{(3.15)}$$

to present the plasmon frequency. It is noted that reducing effective electron density as well as tremendously increasing effective electronic mass would immediately reduce the plasmon frequency for this system. As an example, for aluminum wires ($n = 10^{29}\ m^{-3}$) with $r = 1\ \mu m$

and a = 10 mm, the calculated effective mass value was

$$m_{eff}=2.67x10^{-26}kg\ , \tag{3.16}$$

was almost 15 times heavier than that of a proton, The derived plasma frequency is about 2 GHz, i.e. the structure is a negative dielectric material at microwave frequencies. Note that the final expression for the plasma frequency in equation (3.15) is independent of the microscopic quantities such as the electron density and the mean drift velocity. It only depends on the radius of the wires and the spacing, implying that the entire problem can be recast in terms of the value combination of capacitances and inductances. This approach was used in references [42-43]**,** and it is presented below for the sake of completeness. Consider the current induced by the electric field along the wires, which is related to the total inductance (self and mutual) per unit length (L):

$$E_z=i\omega LI=i\omega L\pi r^2nev\ , \tag{3.17}$$

and the polarization per unit volume in the homogenized medium is

$$P=-n_{eff}er=\frac{n_{eff}ev}{i\omega}=-\frac{E_z}{\omega^2a^2L} \tag{3.18}$$

where $n_{eff}=\pi r^2n/a^2$ as before, one can estimate the inductance, L, by calculating the magnetic flux per unit length, φ, passing through a plane between the wire and the point of symmetry between itself and the next wire where the field is zero: φ,is presented by

$$\varphi=\mu_0\int_r^{a/2}H(\rho)d\rho=\frac{\mu_0 I}{2\pi}\ln[\frac{a^2}{4r(a-r)}] \tag{3.19}$$

Noting $\Phi = LI$, and the polarization $P = (\varepsilon - 1)\varepsilon_0 E_z$, where ε is the effective permittivity, one obtains in the limit $r \ll a$,

$$\varepsilon(\omega)=1-\frac{2\pi c^2}{\omega^2a^2\ln(a/r)} \tag{3.20}$$

The Equation 3.19 is identical to the relation obtained in the plasmon picture. However, one loses the physical interpretation of a low frequency plasmonic excitation here. It is simple to add the effects of finite conductivity in the wires, which had been neglected in the above

discussion. The electric field and the current would now be related by

$$\mathbf{E}_z = i\omega LI + \sigma\pi r^2 I \tag{3.21}$$

where σ is the conductivity, which modifies the expression for the dielectric permittivity to

$$\varepsilon = 1 - \frac{\omega_p^2}{\omega(\omega + i(\varepsilon_0 a^2 \omega_p^2 / \pi r^2 \sigma))} \tag{3.22}$$

Thus the finite conductivity of the wires contributes to the dissipation, showing up in the imaginary part of ε. For aluminum, the conductivity is $\sigma = 3.65 \times 10^7 \Omega^{-1} m^{-1}$, which yields a values of $\gamma = 0.1\omega p$ that is comparable to the values in real metals [44]. Thus the low frequency plasmon is sufficiently stable against absorption to be observable.

In the above discussion, only wires pointing in the *z*-direction were considered. This made the medium anisotropic with negative ε only for waves with the electric field along the z direction. The medium could be constructed to have a reasonably isotropic response by considering a lattice of wires oriented along the three orthogonal directions as shown in figure3-6. In the limit of large wavelengths, the effective medium appears to be isotropic as the radiation fails to resolve the underlying cubic symmetry yielding a truly three-dimensional low frequency plasma.

For very thin wires, the polarization in the direction orthogonal to the wires is small and can be neglected. Thus the waves only sense the wires parallel to the electric field, and correspondingly have a longitudinal mode. The effects of the connectivity of the wires along different directions at the edges of the unit cell have also been examined [9]. A wire mesh with non-intersecting wires was shown to have a negative *ε* at low frequencies below the plasma frequency, but had strong spatial dispersion for the transverse modes above the plasma frequency. This issue of spatial dispersion has been studied more recently by Belov et al [43].

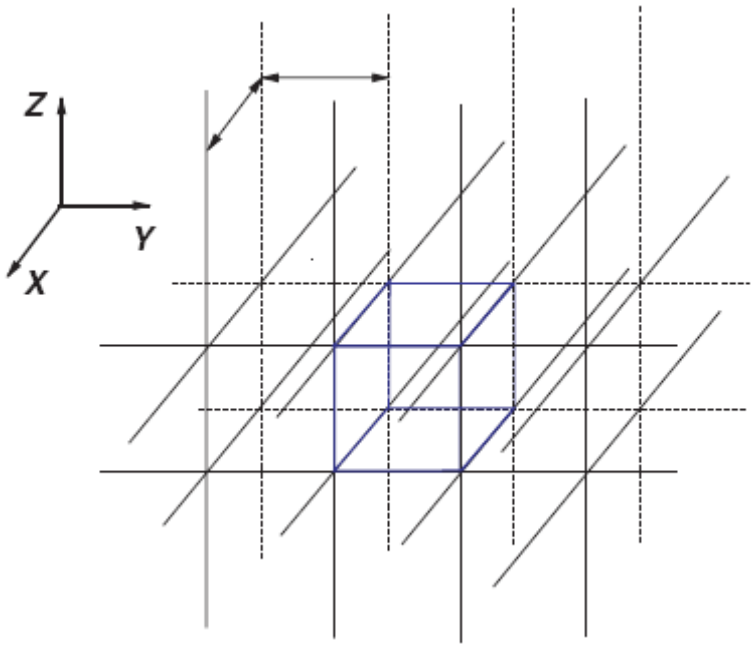

Figure 3-6. A three-dimensional lattice of thin conducting wires behaves like an isotropic low frequency plasma. The figure is imaged from [8].

The continuous wire structure behaves like a high-pass filter, which means that the effective permittivity will take negative values below the plasma frequency. However, for discontinuous wire structures, the negative permittivity region does not extend to zero frequency, and there appears a stop-band around the resonance frequency. In contrary to the continuous wire structures that exhibit a stop-band with no lower frequency edge, the present configuration exhibits a stop-band with a well-defined lower edge due to the discontinuous nature of the wires.

3.4 Composite meta-materials (CMM)

This section is based on the results from last two sections. CMMs (also named as left-handed materials - LHM) combine two parts of negative permittivity and negative permeability simultaneously, in order to have a negative index of refraction. The physical mechanism was presented before. By selecting proper geometric structures of SRR and WIRE

that have been discussed in the proceeding sections, to combine them together through matching of suitable stop-bands, one can compose CMM for mid-IR range.

Chapter 4

Experimental techniques

4.1 Introduction

Experimental techniques and equipments that were used in this thesis work are presented in detail in this chapter. In the following sections, instruments and how these instruments were set up are introduced. A detailed process flow for fabrication of patterns is described, and a method for spectral analyses of FTIR measurements was developed in the section. A suitable way of setting up the experimental instruments is very crucial for effectively extracting the data of measurements and proving further understanding of physics insights.

4.2 Process steps of pattern fabrication

Micro-fabrication of patterns is the key part of the thesis work. The patterns were fabricated on Si substrates, therefore, the transmission measurements at the wavelengths short than 1.2 is prohibited due to strong band-to-band absorption, and the patterns for this study were fabricated by Cu materials. Since to coat a Cu film using either deposition or plating is very complex, in the present work a relative simple and manufacturable technique was developed for making Cu patterns. This technique was a combination to first form backbone of patterns using Si by the CMP process, followed by a chemical substitution reaction to replace Si by Cu. The process flow for such a micro-fabrication procedure is schematically

presented in Figure 4.1, and each step is detailed as follows.

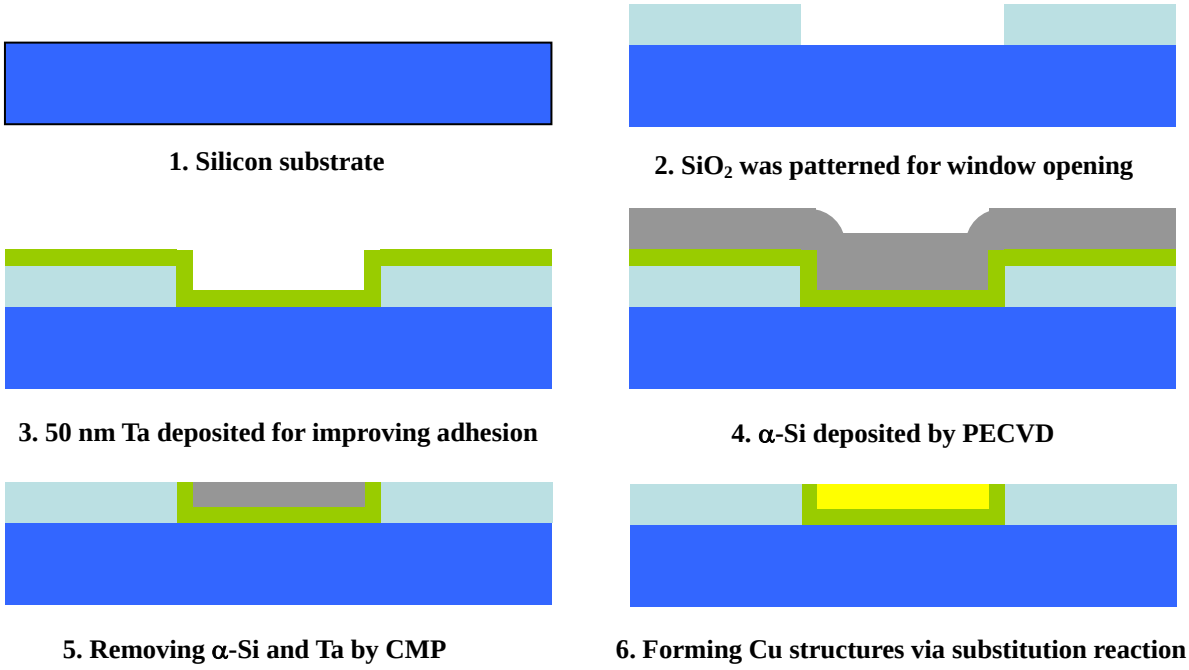

Figure 4-1. Process flow of micro-fabrication

(1) Substrate: For most of experiments 6” Si (100) wafers were used as the substrate, as which was a prerequisite for process equipments in the fabrication pilot line. At the late stage of the work, quartz substrates were also used in order to fabrication some structure to be operated at the visible light spectral range. The major specifications of 6” silicon wafer are listed in the table below：

Diameter(mm)	149.5~150.5	Product	Single side polished
Method	CZ	Type	P
Orientation	1-0-0	Dopant	boron
Thickness(μm)	650~700	Resistivity(Ω-cm)	15~25

Table 4-1. Materials specifications of Si wafers

(2) Thin dielectric film deposition: About 300nm thickness of silicon dioxide (SiO_2) was deposited as a dielectric layer using PECVD. This oxide was served for two purposes. One

was to define the window opening of patterns using lithograph as will be described in the next step, and another was to provide a barrier for separating any copper film which was deposited outside of patters from the silicon substrate.

(3) Window opening: The thin silicon dioxide layer was successively patterned by e-beam lithography (LEICA WEPRINT 200 e-Beam stepper, and have the ability to reproducibly achieve feature sizes below 100 nm, and multilayer lithography with less than 40 nm overlay). Positive resist (PMMA) was chosen for e-beam lithography, and the resist layer was coated by Clean Track MK-8. The geometrical sizes of silicon dioxide patterns using in this work are summarized in Figure 4.2. The oxide through the opening of resist patterns were then removed by ICP dry etching using Larm Tel-5000 etcher.

(4) Tantalum layer deposition: A thin (~50 nm) tantalum layer was then deposited using sputtering over patterned silicon dioxide. Tantalum was used as a buffer layer for improving the adhesion between silicon dioxide and copper during and after copper replacement. It was observed that the copper film was peeled off from SiO_2 when no adhesion layer was used. Actually, 5~10nm tantalum was enough for serving the adhesion purpose.

(5) Si deposition: A amorphous silicon layer, which would be prepared to form the backbone of patterns for copper replacement, was deposited over thin film of tantalum using plasma enhanced chemical vapor deposition (PECVD), because it was demanded for trench filling with a good step coverage. PECVD usually provides better step coverage than conventional CVD and PVD. If step coverage is poor or no amorphous silicon fills into the trenches, copper replacement will be failed.

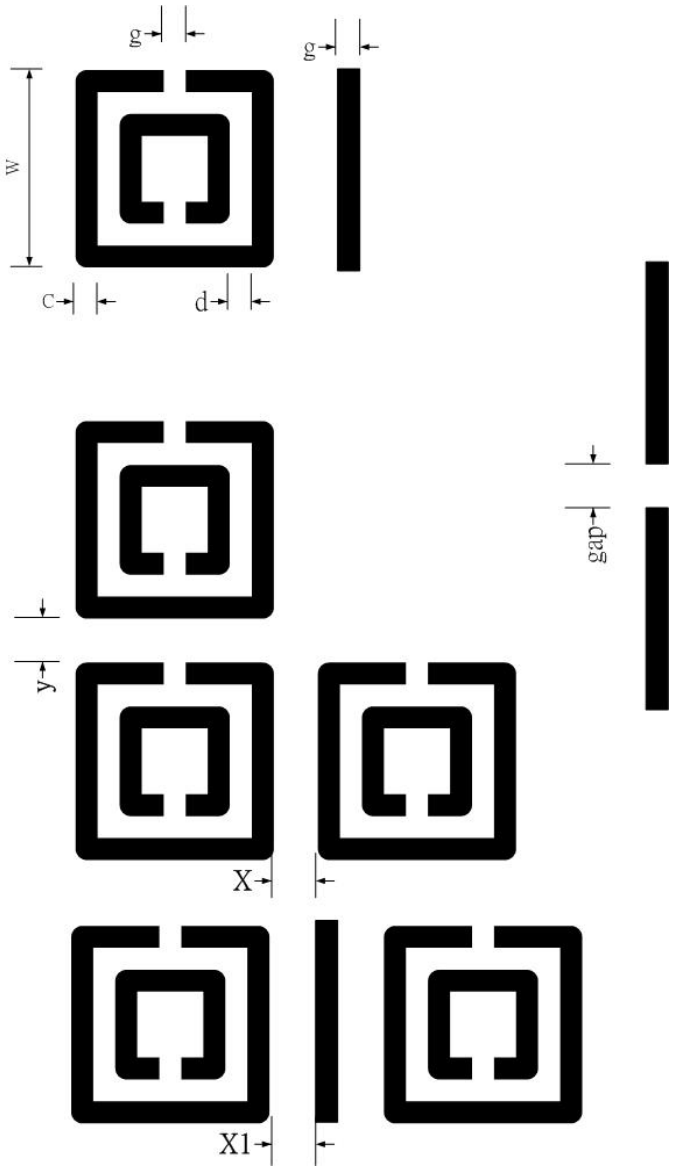

	Type 1 (μm)	Type 2 (μm)	Type 3 (μm)
c	0.18	0.2	0.25
d	0.216	0.24	0.3
g	0.3474	0.386	0.4825
w	1.8864	2.096	2.62
X	0.576	0.64	0.8
Y	0.576	0.64	0.8
gap	0.144	0.16	0.2
X1	0.576	0.64	0.8

Figure 4-2. Geometrical sizes of SRR, WIRE, and CMM patterns.

(6) CMP planarization of patterned surface: α-Si and Ta outside the pattern region were removed through a planarization process using multi-step chemical-mechanical-polishing (CMP). It is very crucial that any residue remained outside the pattern trenches would cause patterns deformation or failure. Therefore, the CMP process should be carefully monitored and controlled, in order to finish it on the SiO_2 surface in the non-patterned region.

(7) Copper replacement: This is the final step through the entire process flow, while this is also the most important step to produce demanded structures with copper (Cu). Since it involves more complicated chemical reactions, it will be described in more detail in the next section.

4.3 Chemical replacement of Cu patterns

In this section, the guidance of copper replacement experimental is given as below. By dipping the wafers in the aqueous bath containing 7.5 g/L cupric sulfate (CuSO4) and 1% buffered oxide etch (NH4F/HF mixture in 6:1 volume ratio) diluted with 99% deionized (DI) water at an ambient temperature, a substitution reaction between the Si backbone structures and Cu electrolyte occurs such that Cu could be selectively formed in the patterns region instead of Si. The chemical replacement is carried out through a chain of following reactions.

The contact displacement is conducted by means of the electrochemical redox between Si^0 and Cu^{2+} ions in an aqueous solution containing F^- ions, as shown in Equation. 4.1~4.3 [46-48]

Anode $$Si_s + 6F^-_{aq} \rightarrow SiF^{2-}_{6\ aq} + 4e \quad \textbf{(4.1)}$$

Cathode $$Cu^{2+}_{aq} + 2e \rightarrow Cu_s \quad \textbf{(4.2)}$$

Overall $$Si_s + 6F^-_{aq} + 2Cu^{2+}_{aq} \rightarrow 2Cu_s + SiF^{2-}_{6\ aq} \quad \textbf{(4.3)}$$

The electrochemical redox reaction involves the oxidation of one Si atom to release four electrons and reduce two cupric ions to two Cu atoms. The oxidized Si^{4+} ions would be stabilized with the fluoride ions to form soluble SiF_6^{2-} ions in the aqueous solution, not forming passivating silicon oxide with water that would inhibit the following redox reaction.

The thickness growth of the replaced Cu would be almost 1.5 times larger than that of the consumed α-Si thickness on average. The substitution rate of Cu was approximately 100 nm/min in the initial stage, but dropped to 75 nm/min after 3 min displacement. This may be due to the mass transfer inhibition of the oxidized SiF_6^{2-} species out and fluoride ions in process through the top replaced Cu layer, but weakly relating to the cupric ions, which were only diffused and reduced onto the Cu surface from bulk solution. This thus turns out to be an advantage for the Si CMP process. However, it would be filled with Cu in the trenches after completing contact displacement. This could significantly relax the process window for Si CMP to insure over-polishing against complete removal of α-Si outside the trench and the selectivity of the Cu contact displacement. [49-50]

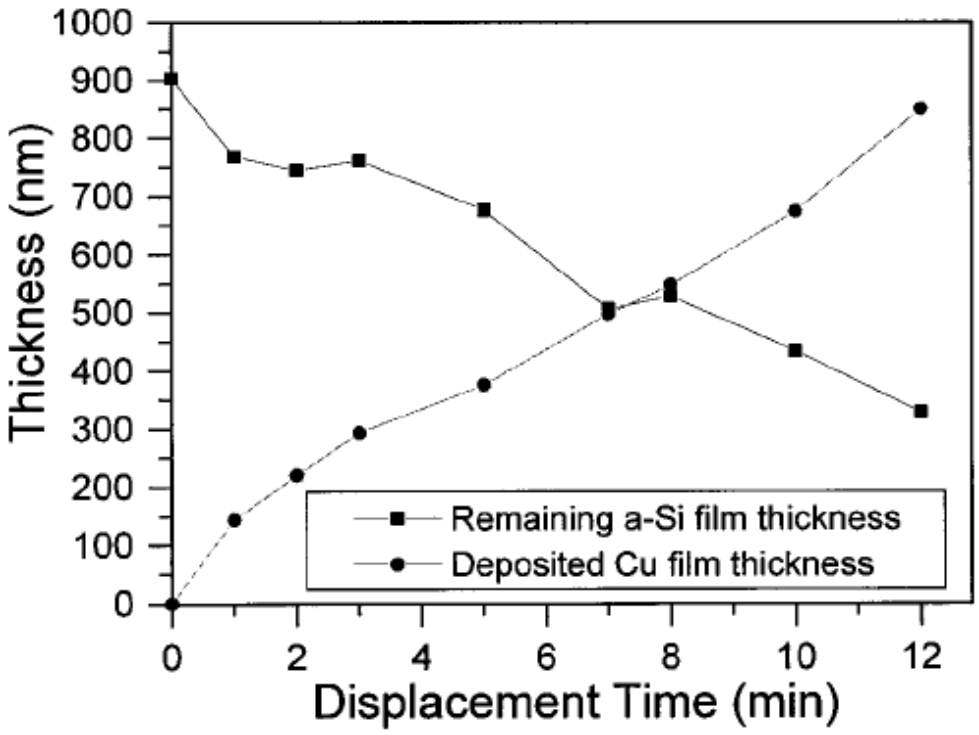

Figure 4-3. Thickness changes of the substitutional Cu and the consumed α-Si films during contact displacement at 30°C. The figure is imaged from [45].

The SEM micrographs of patterns after Cu replacement are depicted in Figures 4.4-4.6.

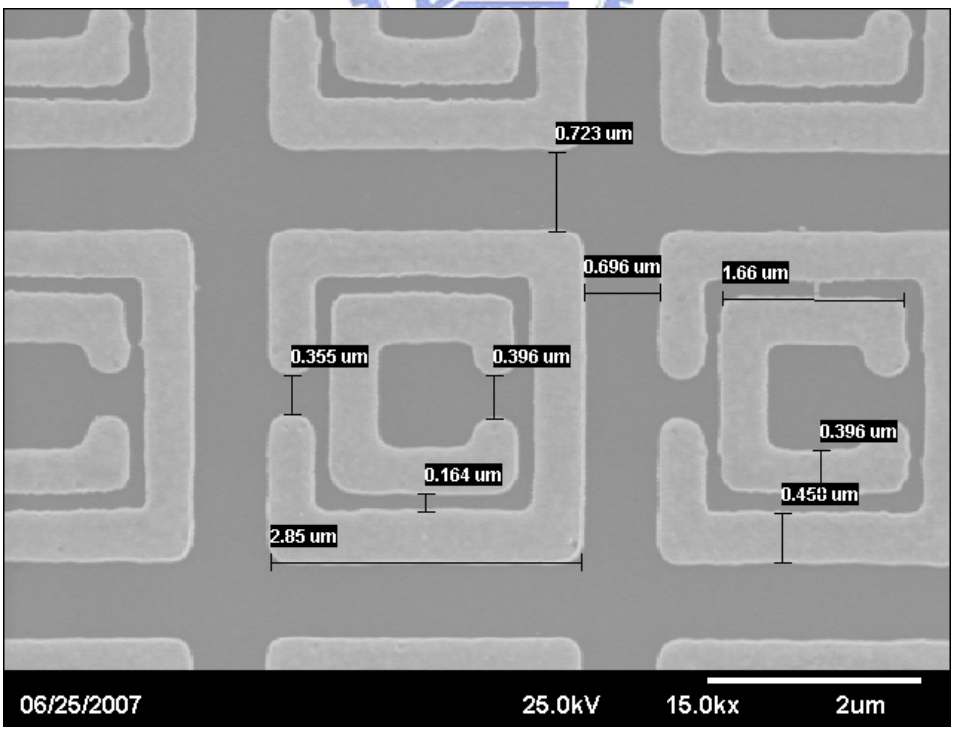

Figure 4-4. A SEM image of SRR after Cu replacement.

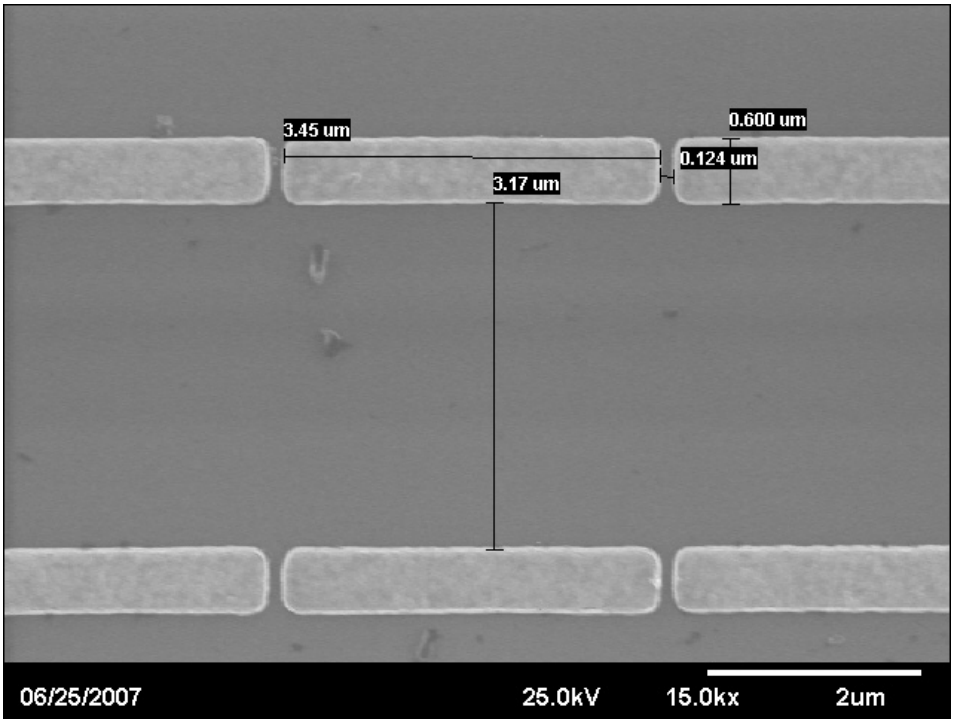

Figure 4-5. A SEM image of WIRE after Cu replacement.

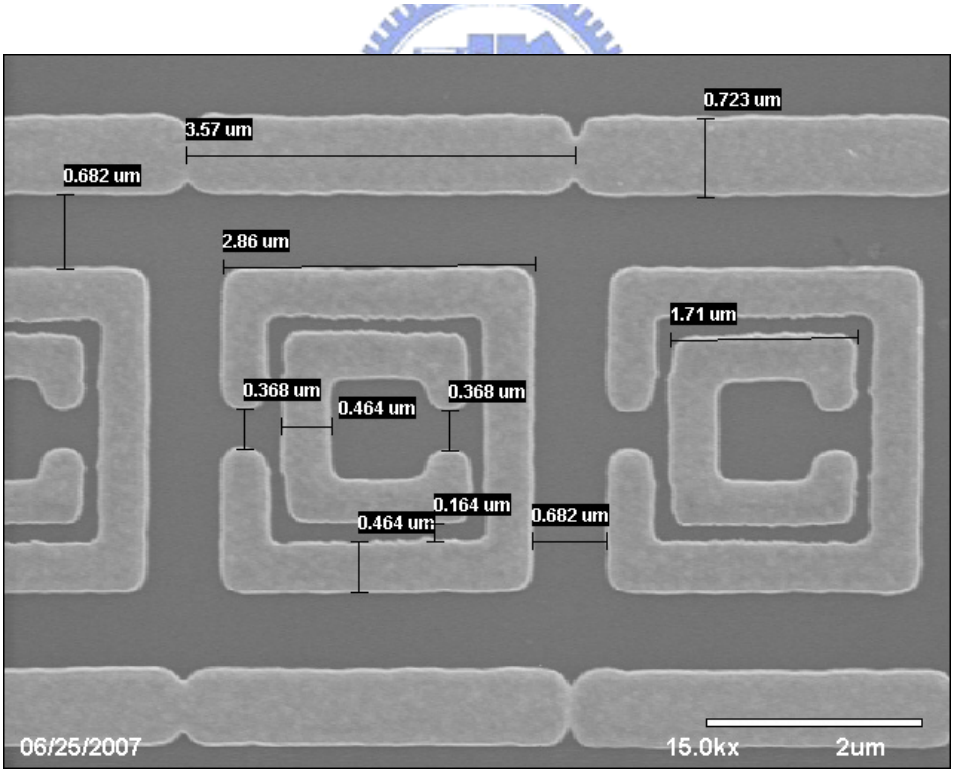

Figure 4-6. A SEM of LHM after Cu replacement.

EDX measurements were successively performing in order to ensure complete removal

of Cu outside of the pattern trench region. The EDX spectra are shown in Figures 4-7(a) ~4-7(c)

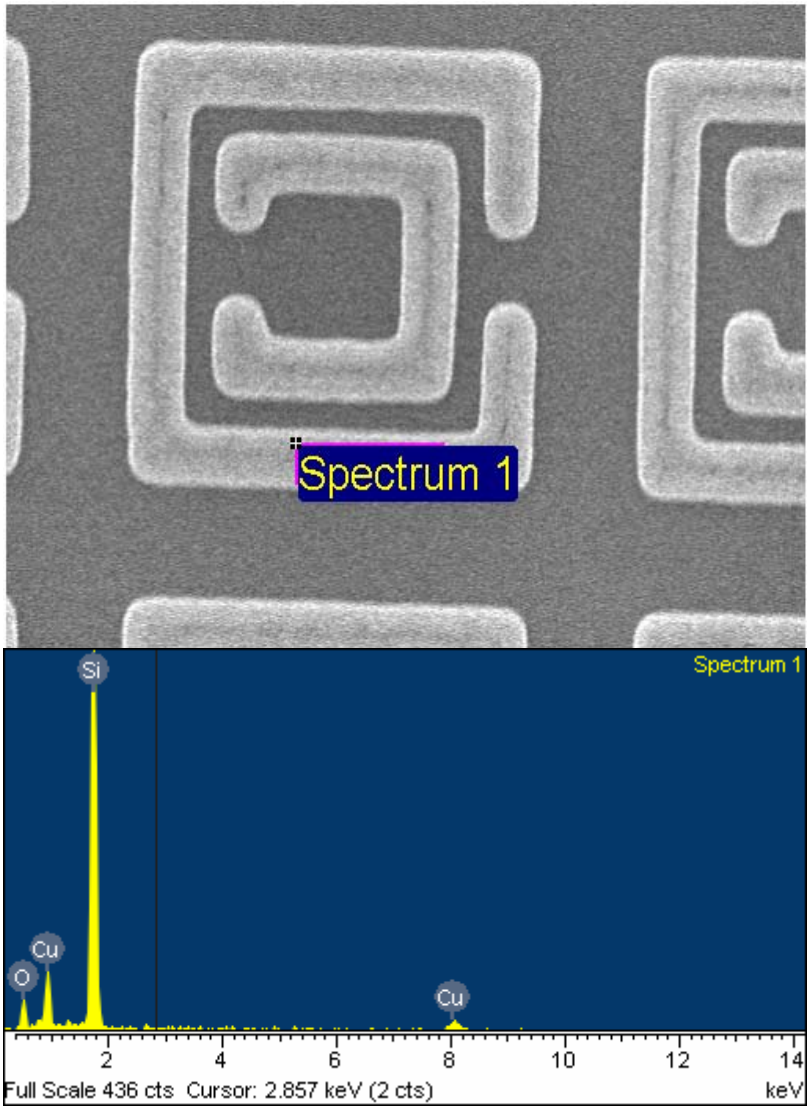

Figure 4-7(a). EDX spectrum of SRR at a measurement point over outer split ring.

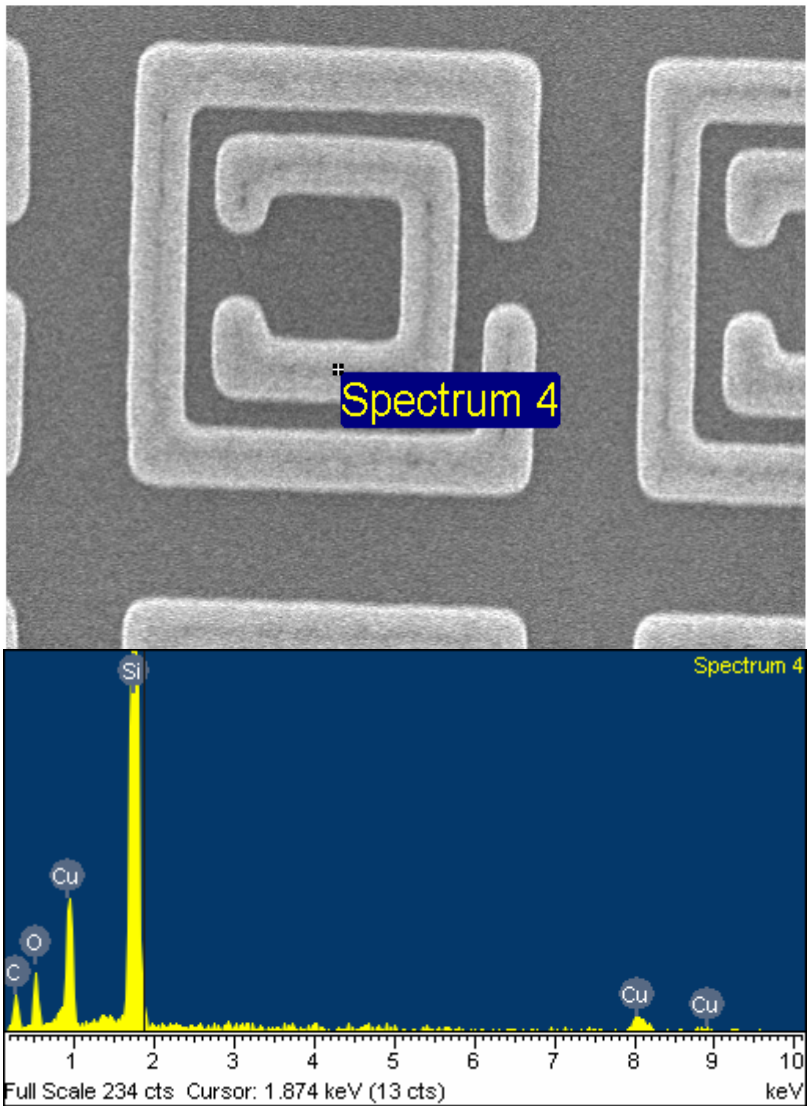

Figure 4-7(b). EDX spectrum of SRR at a measurement point over inner split ring.

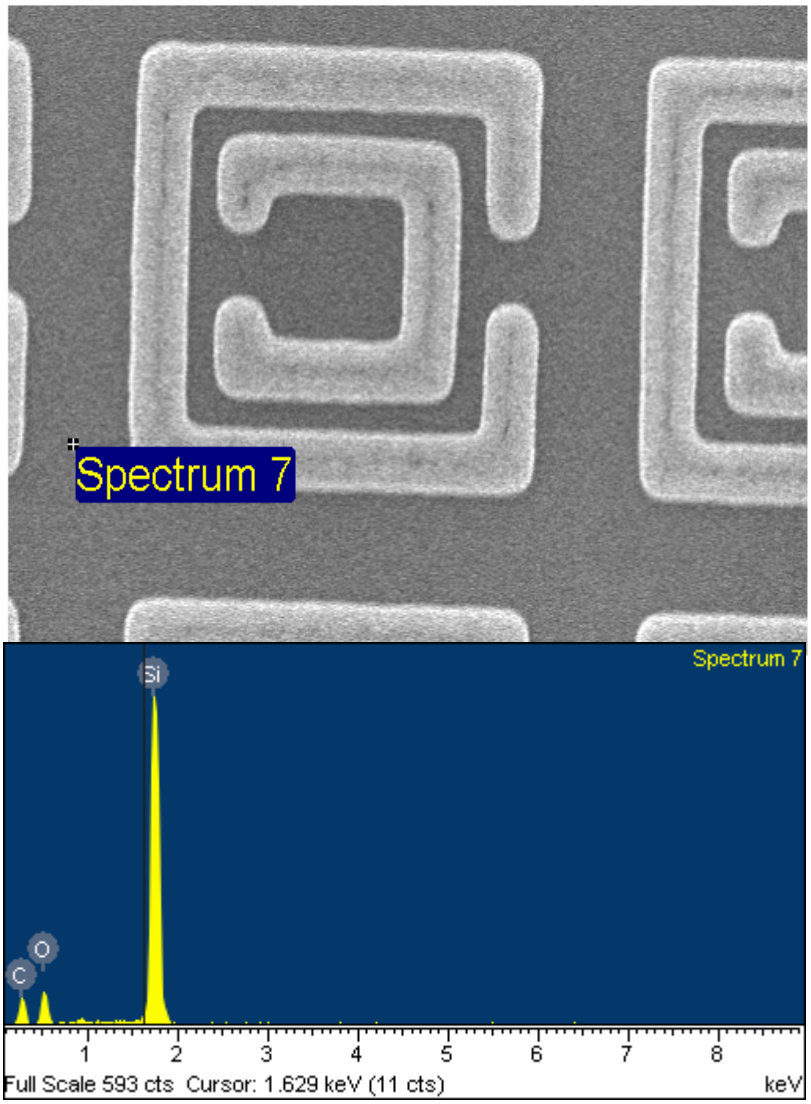

Figure 4-7(c). EDX spectrum of SRR at a measurement point outside the trench.

4.4 Optical characterization of meta-materials

Optical experiments were performed using Fourier Transformation Infrared Spectrometry (FTIR), Vertex 70 made by BRUKER™. This instrument provides means for spectroscopic analyses of E.M. waves interacting with materials and patterns. The optical path in Vertex 70 is schematically illustrated in Figure 4.8.

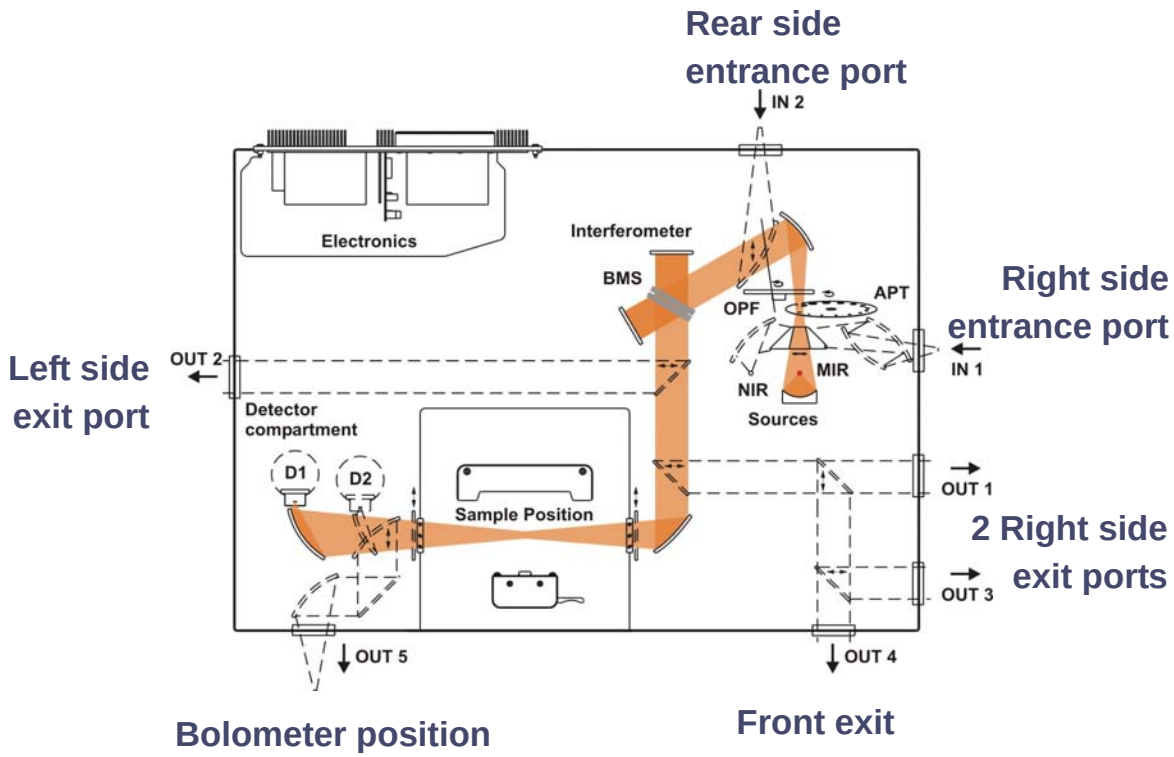

Figure 4-8. Optical path runs in BRUKER™ Vertex 70. Figure is imaged from BRUKER™

A more detailed drawing depicts how E.M waves incident onto the sample stage is shown following Figure 4-9：

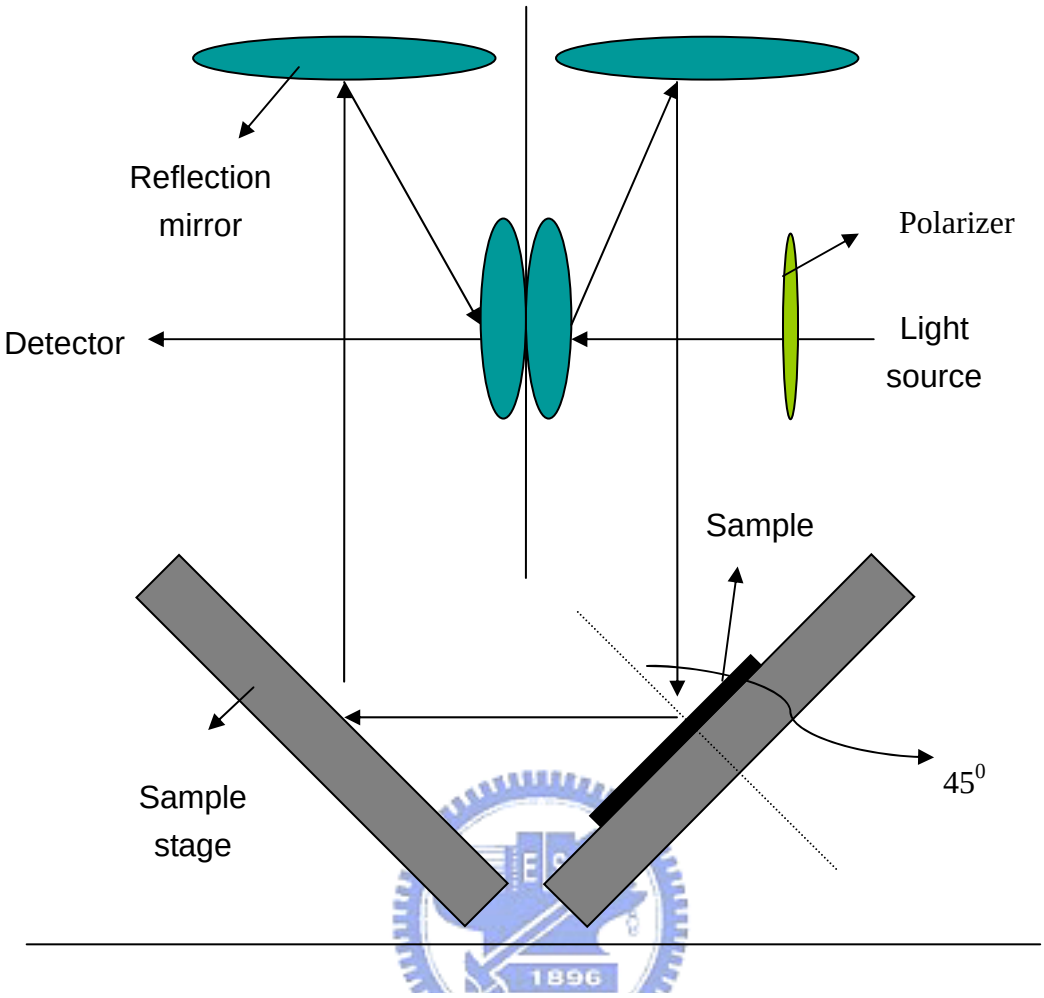

Figure 4-9. Optical path for light runs from light source to detector. The pattern array is placed on the sample stage.

During the measurements, the patterned sample was placed on the sample stage and angles of the incident light were 45° with respect to the sample surface normal for all experiments. It is difficult to perform measurements at an incident angle of 90°, although the most favorable measurement geometry to introduce magnetic resonance of SRR is to set the H field normal to the plane of patterns (i.e. s-polarization, incident angle=90°). The polarization of light can be adjusted by polarizer to set the E-field vector either normal (p-polarization or TM-mode) or parallel (s-polarization or TE-mode) to the pattern surface.

Vertex 70 has a wide spectral detection range from mid-IR through near-IR to visible light. For patterns processed for the thesis work, the resonance frequency is expected to appear at mid-IR. So a MCT detector was used to cover the spectral range from k=600^{-1}

cm~7500^{-1} cm.

4.5 Procedure for Spectral normalization

In order to reduce the influence from layer interferences and to highlight the features that are interested for study, some procedures for spectral normalizations were employed during the data analyses and discussion. These normalization procedures are introduced, as below:

1. Intensity normalization： Because the intensity of the incident light varies with polarization angles, there is a need to normalize the measured signal intensity with the incident beam at different polarization angle. This was done as follows: (i) First to figure out the spectral (wave-number) ranges in which negative permittivity/permeability are expected to observe by tuning polarizer. (ii) Then to pick a spectral window to draw a slope from lowest point to highest point.(highest point is averaged since it is often very noisy) (iii) From this step, the intensity of signals is normalized, which thus makes the lower intensity to compare to the higher intensity with a meaningful reference. The procedure is figured as follow：

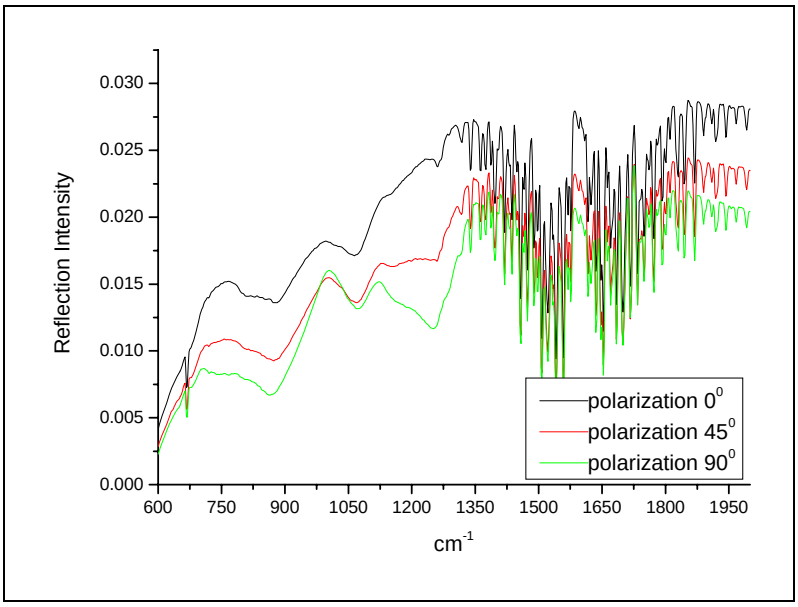

Figure 4-10. Original reflection signals of SRR with three degrees of polarization.

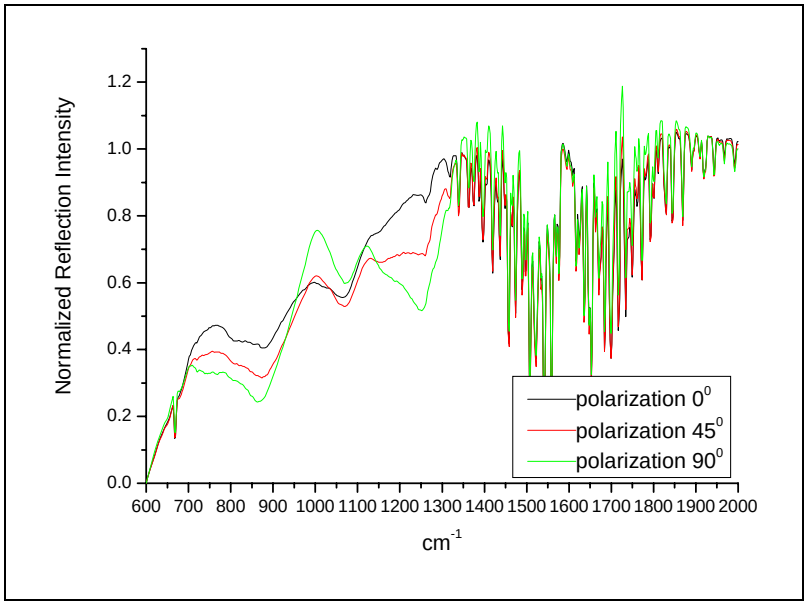

Figure 4-11. Normalized reflection signals of SRR with three degrees of polarization.

2. Suppressing other signals that was not interaction due to pattern and light： This is an effort trying to highlight spectral features that are caused by interactions between the incident light and patterns, while to reduce some features that maybe introduced by interference due to layers on substrate as a general background. Therefore the measured spectrum patterns need to be normalized to the spectrum measured outside of the pattern region. Primary signals are defined as normalized reflection signals of patterns. Secondary signals are defined as normalized reflection signals of background (i.e. the spectrum measured outside of the pattern region). Reflectance can be present as primary signals divided by secondary signals. The procedure is figured as follow：

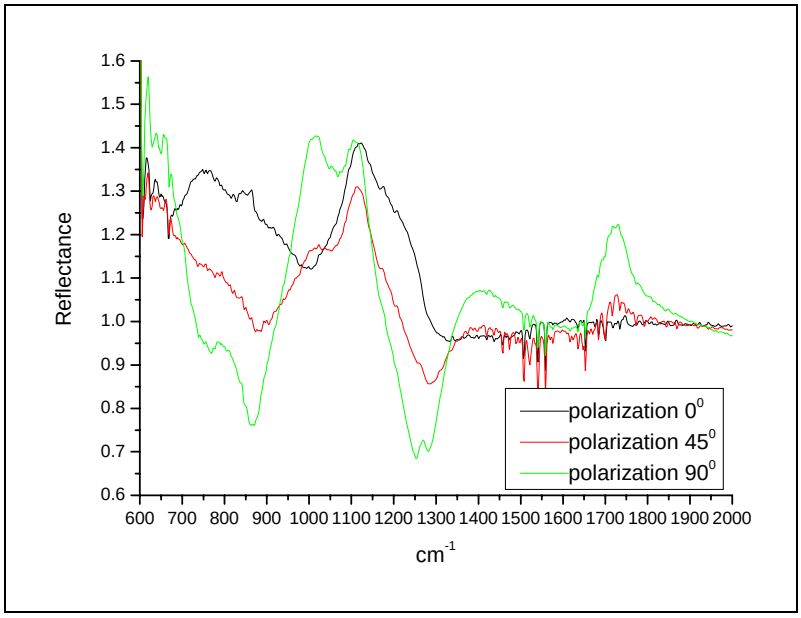

Figure 4-12. Reflectance of SRR with three degrees of polarization.

3. Normalization respect to the polarization effect： This a way to evidently reveal how some effects would be introduced by incident EM waves with different polarizations. For example, the light impinging with s-polarization, i.e. the H vector perpendicular to the pattern surface could excite magnetic dipoles to produce artificial magnetism. But this will not be an effect for the light of p-polarization, i.e. the H vector lies in the plane of the pattern surface. Therefore, the final presentation will be the spectrum measured with s-polarization to divide that measured with p-polarization, in order to increase the contract of the effect. The procedure is figured as follow：(0^0 polarizations is s-polarization and 90^0 polarization is p-polarization)

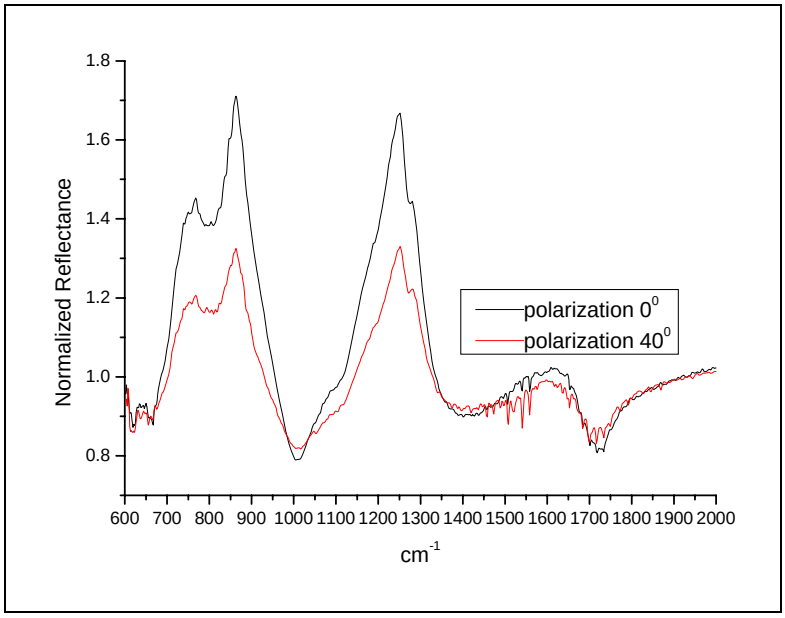

Figure 4-13. Normalized reflectance of SRR.

Chapter 5

Experimental results

5.1 Introduction

In this chapter the experimental results obtained from three types of patterns, namely SRR, WIRE, and CMM, are presented and discussed. The experimental details on optical measurement flowchart as well as data processing and analyzing have been described in the preceding chapters. Here, a brief description of the data processing is summarized again. In the first step “Intensity normalization”, a slope for normalizing the reflection intensity was drawn in a proper spectral (wave-number) range. And for the second step, the spectrum of the patterned sample was normalized the one taken from the region outside of patterns. Finally, for the third step the spectrum measured with s-polarized (or p-polarized) light was divided by one obtained by anther polarization, in order to highlight the significant features that were produced by incident EM waves. Below are results obtained throughout the thesis project work.

5.2 Spectral intensity calibration of optical measurements

The optical measurements of SRR, WIRE, and CMM pattern structures were carried out using FTIR in the reflection experimental geometry. The measurements were performed with different polarization of the incident light from TE to TM modes. Since the optical power of the impinging light varies at different moralization angles and the intensity of measured

spectra should be calibrated and normalized to the input optical power.

In this experiment, five different polarization degrees: 0°, 22.5°, 45°, 77.5°, and 90° were tested with a fix incident angle of light at 45° for all measurements. The aperture slit size for limiting the light shining area was set to ~ 1 mm as default. The results of optical measurements are presented as following：

5.2.1 Optical measurements of SRR

As schematically illustrated in Figures 5-1 and 5-2, the so-called type I arrangement of SRR is to align the incident light along with all splits of ring patterns, and the type-II arrangement means the light azimuth point to the edge with no splits (90° rotation).. In both cases, the incident light is arranged with the E vector lied in the pattern plane, i.e. s-polarization (defined as polarization degree = 0°). In the figure, Y-axis is normal to patterns, and X-Y plane lies in plane of patterns.

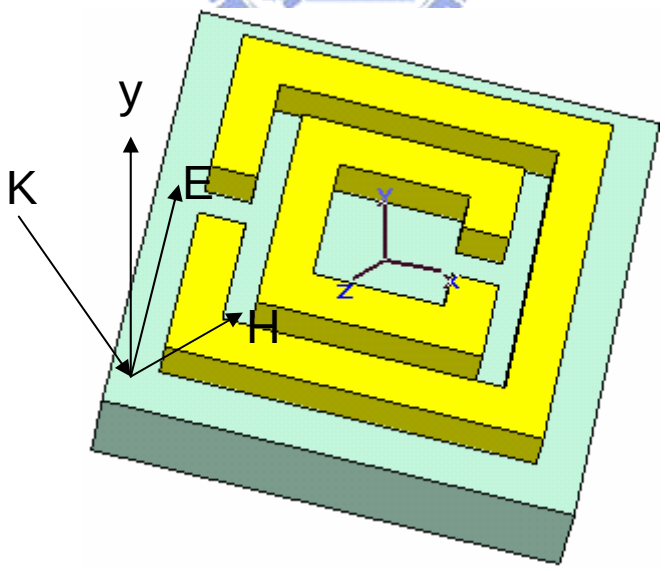

Figure 5-1. Polarization of light for type I arrangement of SRR when E parallel to the pattern is defined as polarization degrees = 0°.

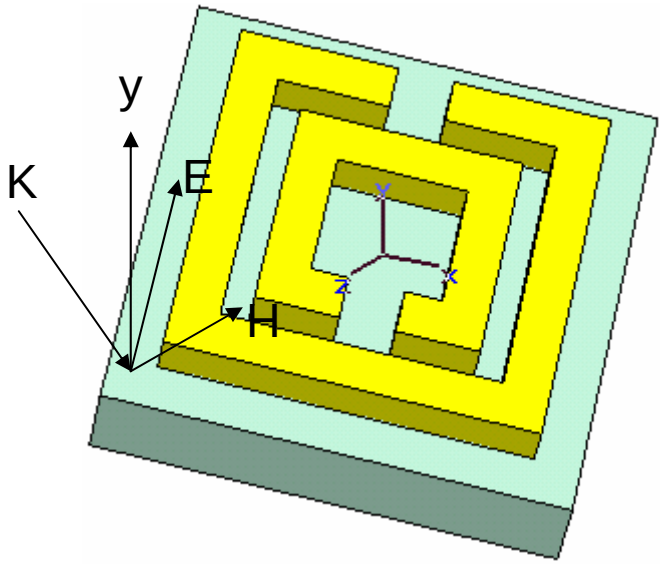

Figure 5-2. Polarization of light for type II arrangement of SRR when E parallel to the pattern is defined as polarization degrees = 0°.

Reflection spectra measured from a SRR sample with type I (Figure 5-3) or type II (Figure 5-4) arrangement, as well as from the area with no patterns (Figure 5-5). The spectral intensity was calibrated with respect to the incident light intensity for three different polarization angles.

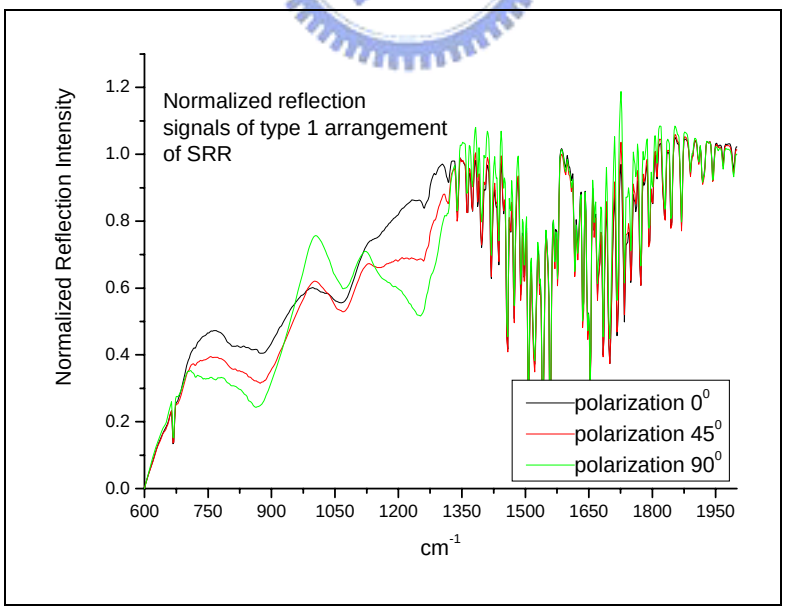

Figure 5-3. Reflection spectra of type I arrangement of SRR with three polarization angles.

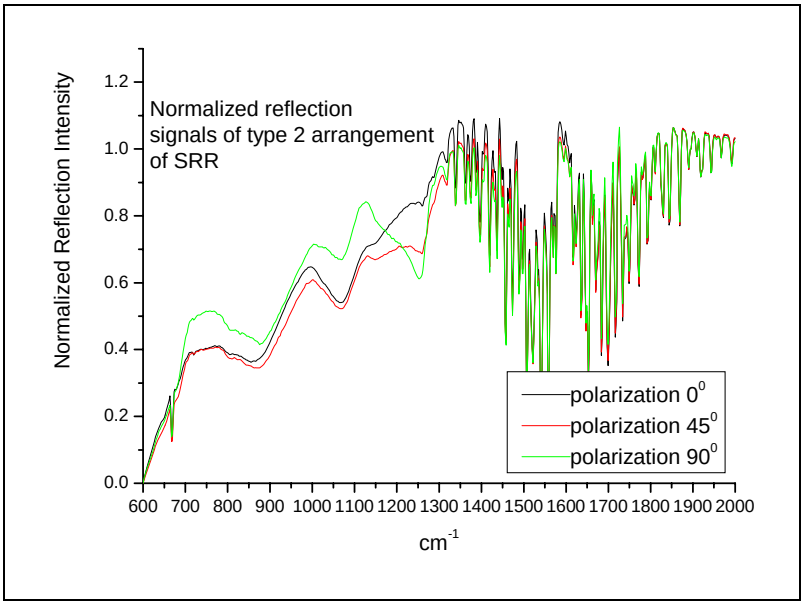

Figure 5-4. Reflection spectra of type II arrangement of SRR with three polarization angles.

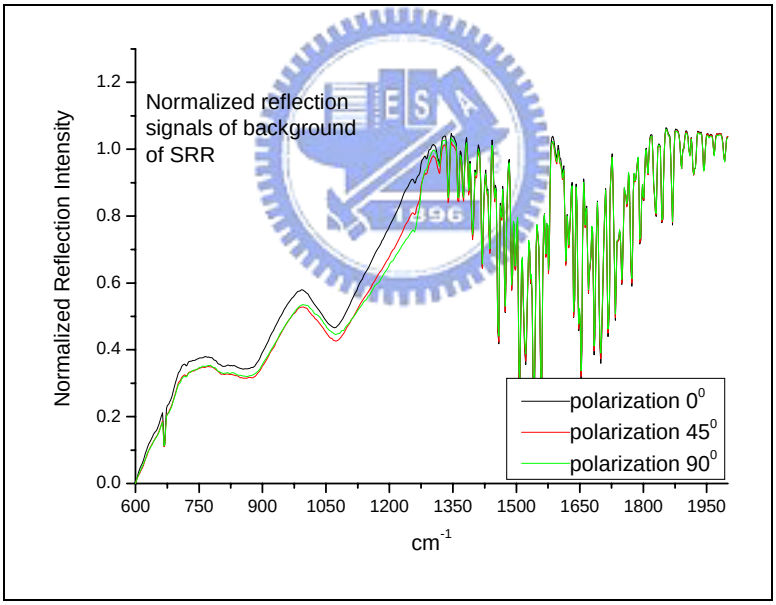

Figure 5-5. Reflection spectra of background of SRR with three polarization angles.

5.2.2 Optical measurements of WIRE

The same as the measurements of SRR patterns, there are also two types of arrangements for optical measurements of WIRE samples. As illustrated in Figures 5-6 and 5-7, the type I or II arrangement of WIRE are to align the incident light either along short or

long side of WIRE patterns, respectively.

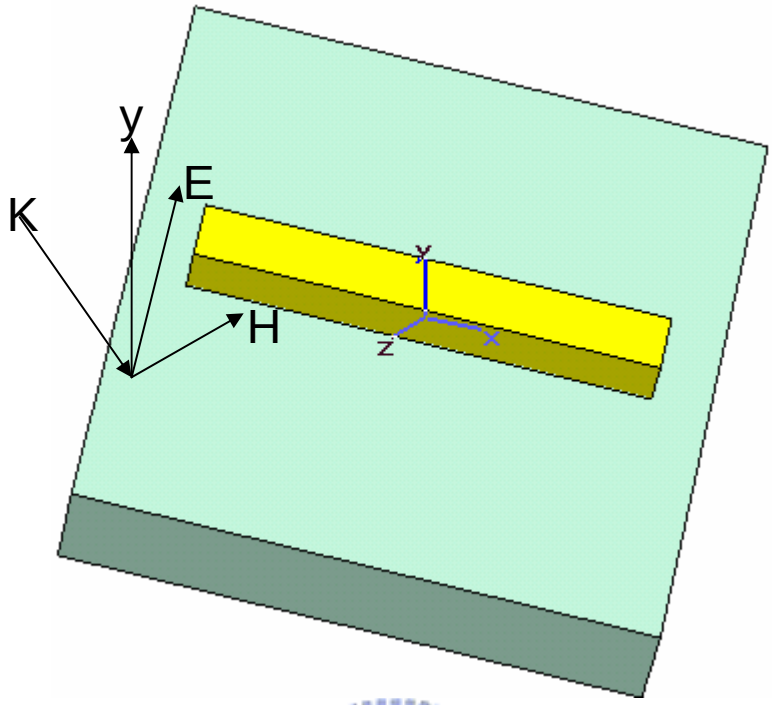

Figure 5-6. Polarization of light for type I arrangement of WIRE when E parallel to the pattern is defined as polarization degrees = 0°.

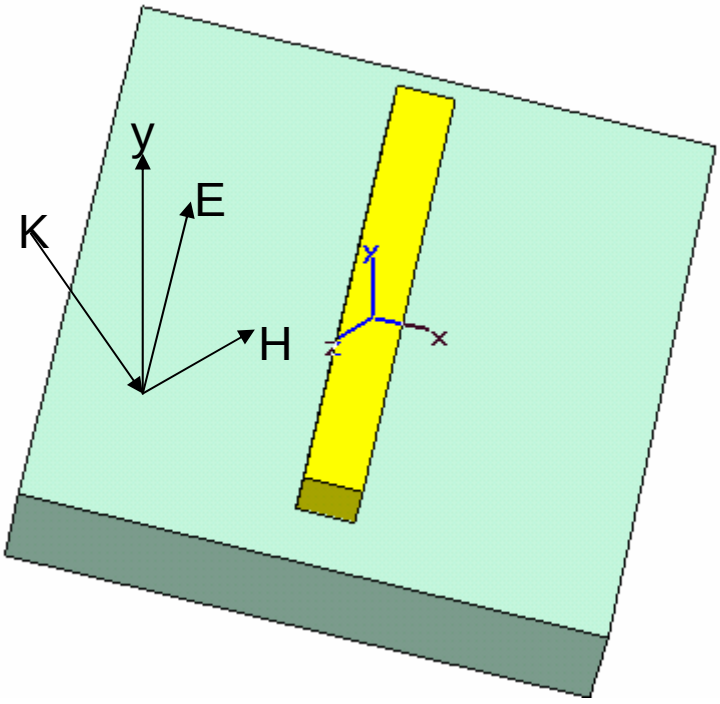

Figure 5-7. Polarization of light for type II arrangement of WIRE when E parallel to the pattern is defined as polarization degrees = 0°.

The measured spectra with type I or type II arrangement and from the no pattern area (reference) are depicted in Figure 5-8, 5-9, and 5-10, respectively. The spectral intensity was calibrated with respect to the incident light power, at three polarization angels.

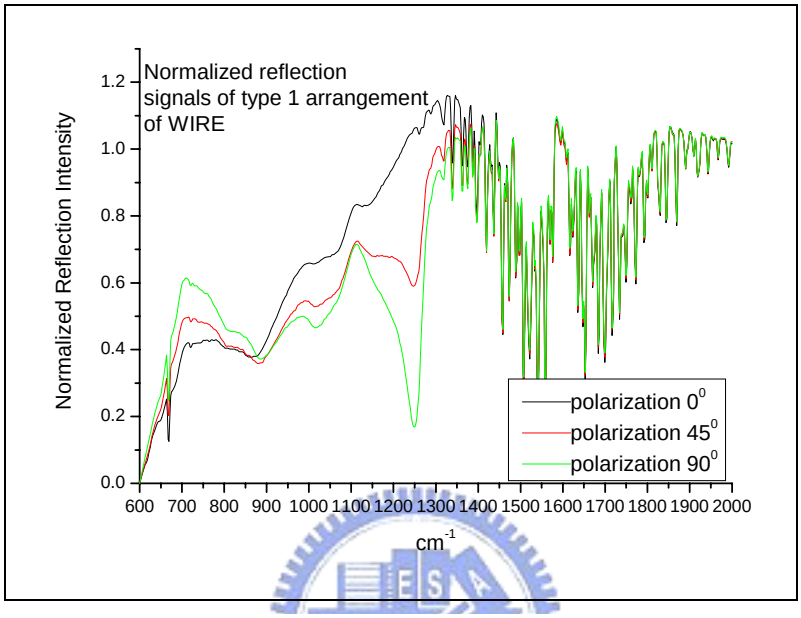

Figure 5-8. Reflection spectra of type I arrangement of WIRE with three polarization angles.

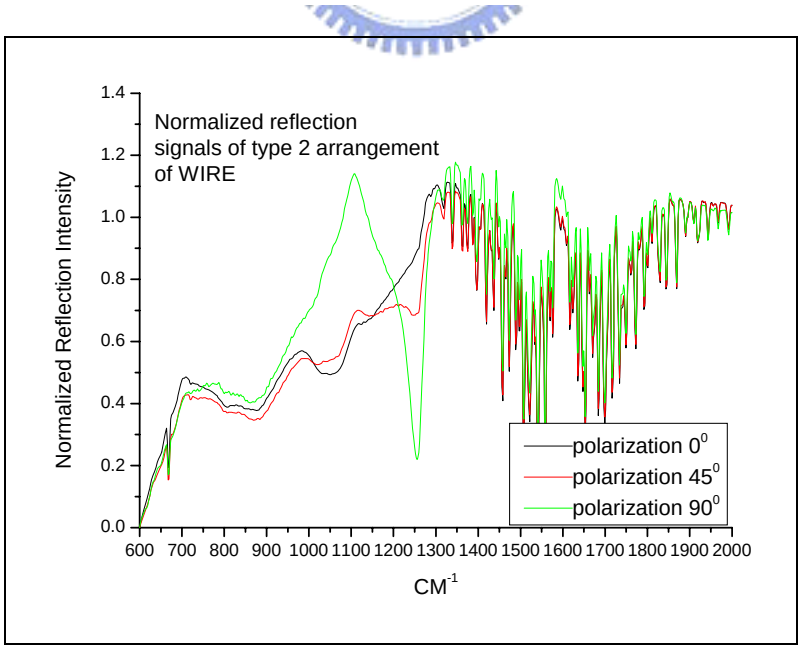

Figure 5-9. Reflection spectra of type II arrangement of WIRE. with three polarization angles.

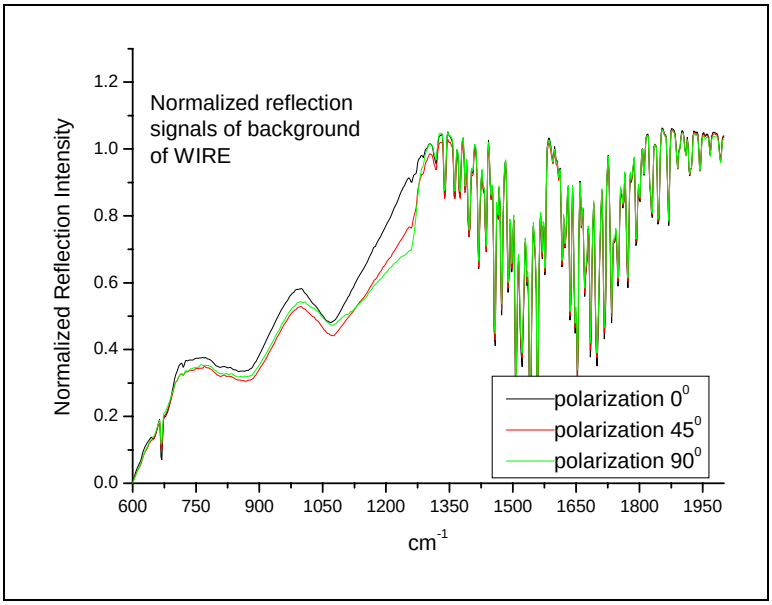

Figure 5-10. Reflection spectra of background of WIRE with three polarization angles.

5.2.3 Optical measurement of CMM

Figure 5-11 and 5-12 illustrate the experimental geometries for type I or II arrangement of CMM.

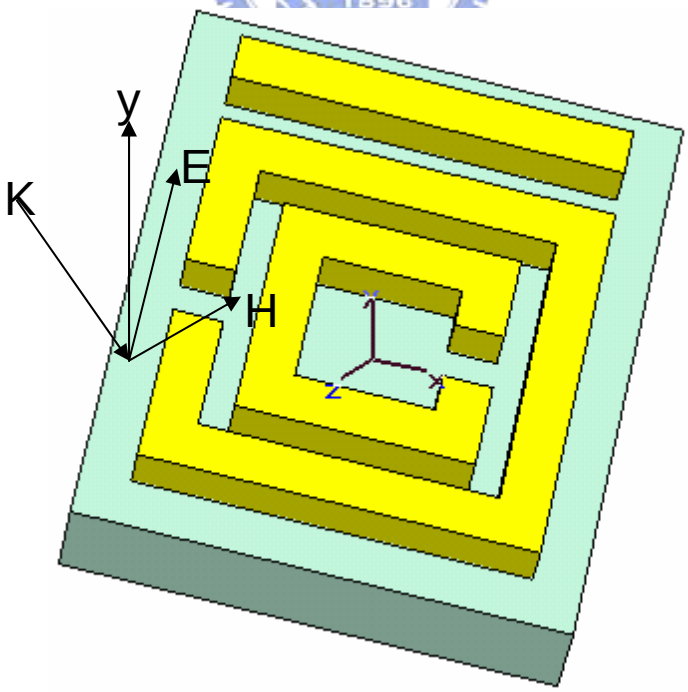

Figure 5-11. Polarization of light for type I arrangement of CMM when E parallel to the pattern is defined as polarization degrees = 0°.

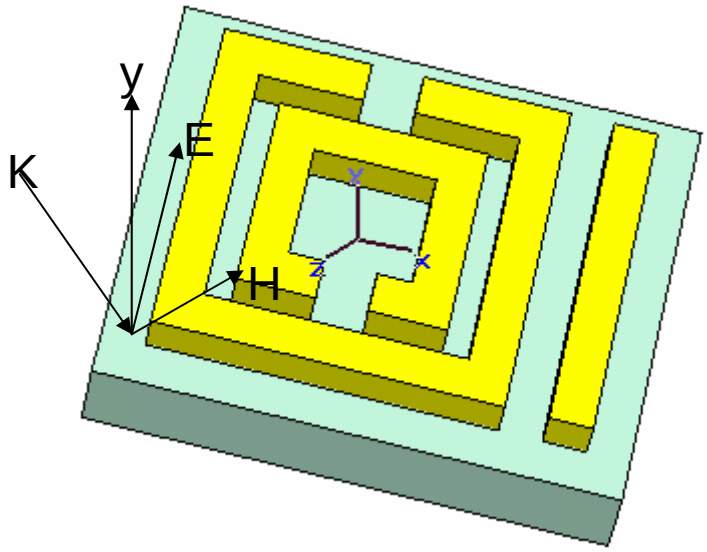

Figure 5-12. Polarization of light for type II arrangement of CMM when E parallel to the pattern is defined as polarization degrees = 0°.

Intensity normalization

Figures 5-13, 5-14, and 5-15 show the measured reflection spectra of CMM, after calibration with input light power, at three polarization angles

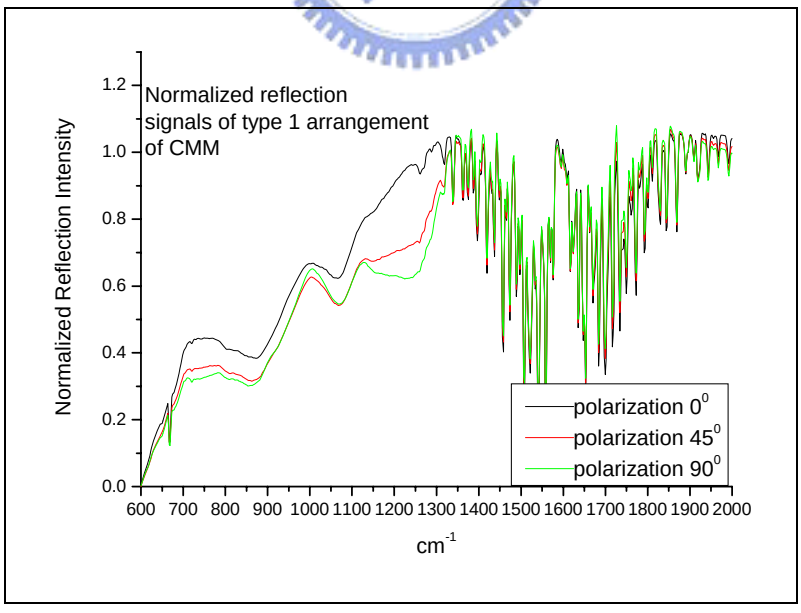

Figure 5-13. Reflection spectra of type I arrangement of CMM with three polarization angles.

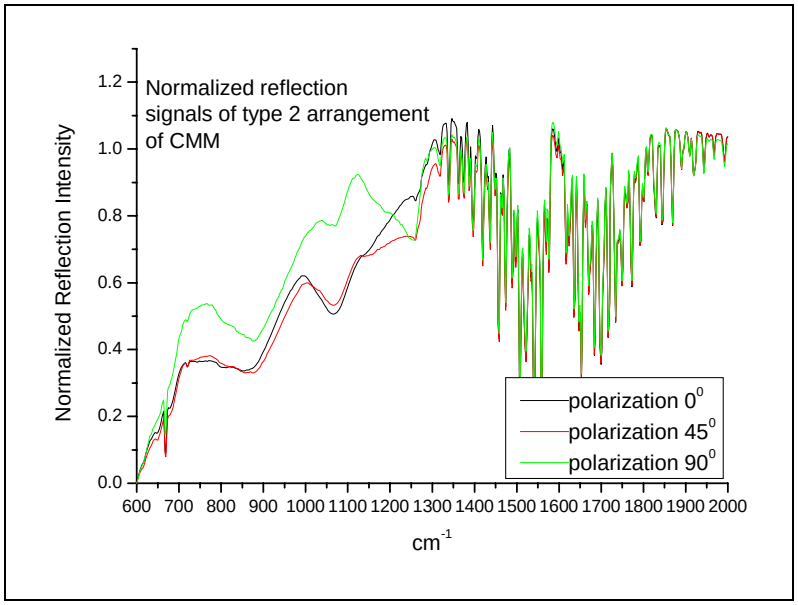

Figure 5-14. Reflection spectra of type II arrangement of CMM with three polarization angles.

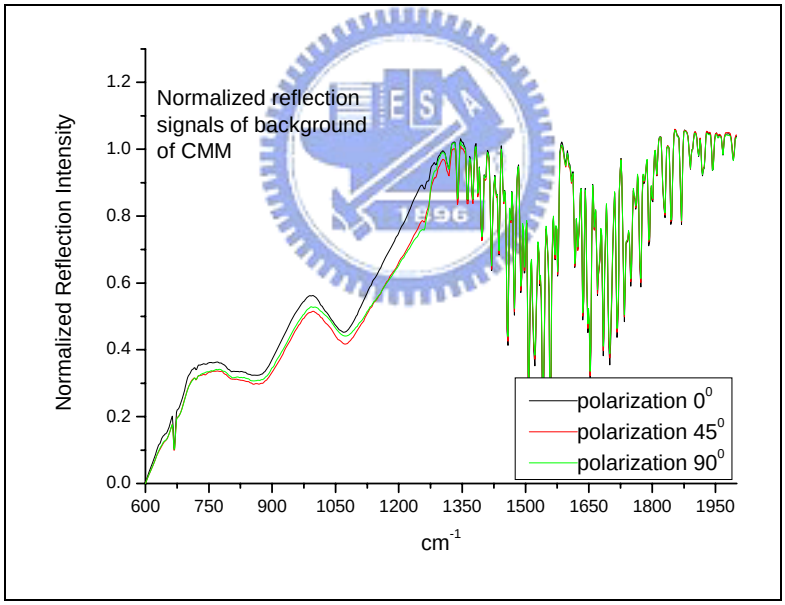

Figure 5-15. Reflection spectra of background of CMM with three polarization angles.

5.3 Spectral processing and analyses

In this section, the reflection spectra after intensity calibration with respect to the incident light power at 3 polarization angles (section 5.2) are further processed and analyzed, in order to remove some inference features that were introduced due to the thin oxide layer on

the substrate, and also to clarify the effects to be introduced by s- or p-polarization of the incident light, i.e. EM waves. For the first effect, the spectra normalization with respect to the one obtained outside the pattern region were employed. The final appearance of any reflection spectrum was actually a ratio of the s-polarized spectrum divided by the corresponding p-polarized spectrum, such that the contribution to the optical reflectance could be identified.

5.3.1 Spectra of SRR

Step1. Reflectance

The procedure was completed by dividing the spectrum from the pattern region with the spectrum from outside of the pattern region in the denominator. The figure only shows the spectra of 0° polarizations.

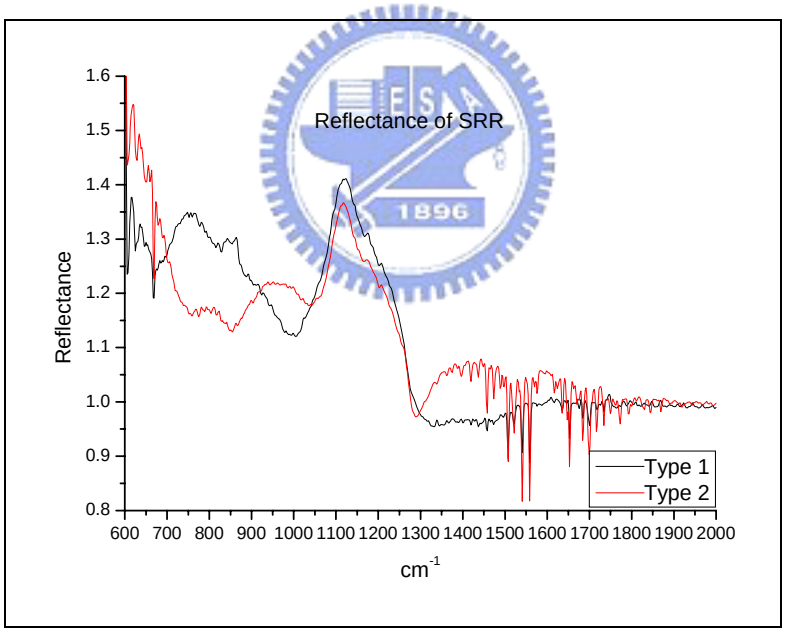

Figure 5-16. Type I and II arrangement of SRR's reflectance.

Step2. Normalized Reflectance

In order to increase contrast between s- and p-polarization effects, the spectrum measured with s-polarization (0 degree) was divided one measured with p-polarization (90 degree). Because with the p-polarized light, the vector of H-field was lying in the plane of

SRR patterns and parallel to the pattern edge with split, so it is unable to excite magnetic dipole for the enhanced reflectance.

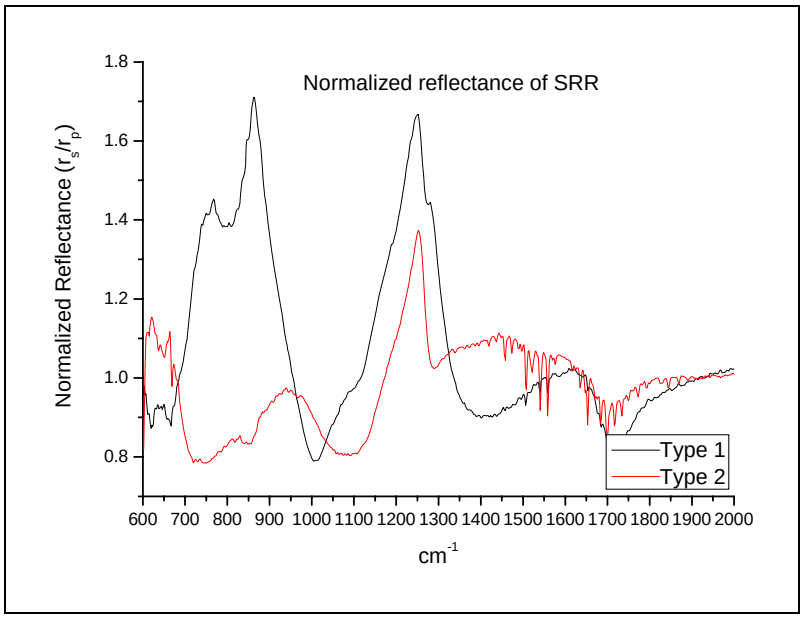

Figure 5-17. Type I and II arrangement of SRR's normalized reflectance.

Discussion

Some important features and possible physics mechanisms behind them are discussed as below.

Three major features are observed on Figure 5-17

1. k=767.6cm^{-1} (f=23.03THz) and k=864cm^{-1} (f=25.92THz) for type I.

2. k=825.51cm^{-1} (f=24.76THz) and k=941.24cm^{-1} (f=28.237THz) for type II .

3. k=1250cm^{-1} (f=37.5THz) exist for each type.

According to ref. [51], it shows that there are three resonance dips for transmission (first dip due to R-C structure of outer split ring, second dip due to inner split ring, and third dip due to electric cut-wire response of the outer ring of its longer side). From the experiment, only two peaks of resonances (i.e. second dip is merged by firs dip and third dip) were

observed for each of two types. Because the strength of this resonance was sometimes very small, it shows that the magnetic response of the inner ring was screened by the presence of outer one [51]. There was another property that was interest in the figure, i.e., electric coupling to the magnetic resonance of SRR [42]. Because type I is E field asymmetry to SRR, it can excite more obvious and wider feature of resonance than type II which is E field symmetry to SRR.

Note that at K=1250cm^{-1} there was a reflection feature existed in every spectrum, which has hereby been attribute to the residual silicon dioxide layer over the Si substrate. This oxide layer is necessary, in order to stop Cu replacement reaction with the Si substrate.

5.3.2 Spectra of WIRE

Step1. Reflectance

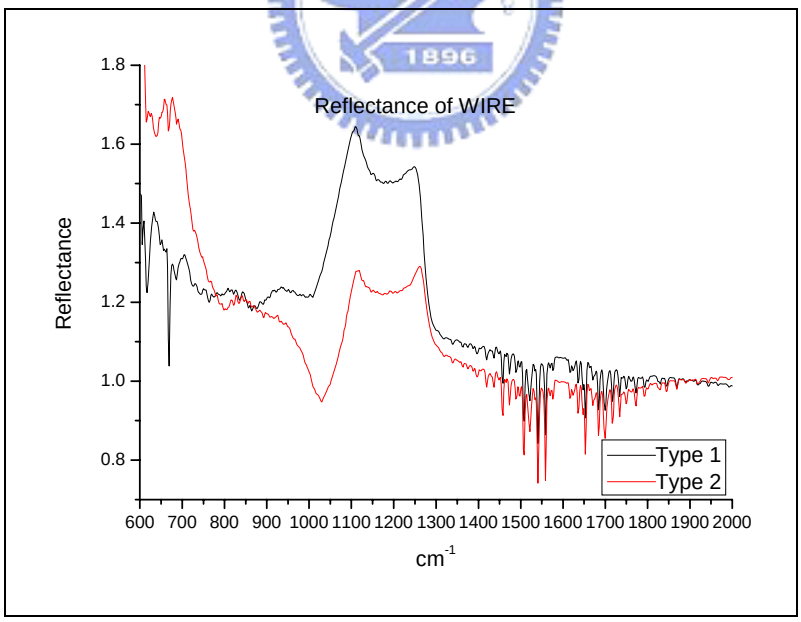

Figure 5-18. Type I and II arrangement of WIRE's reflectance.

Step2. Normalized Reflectance

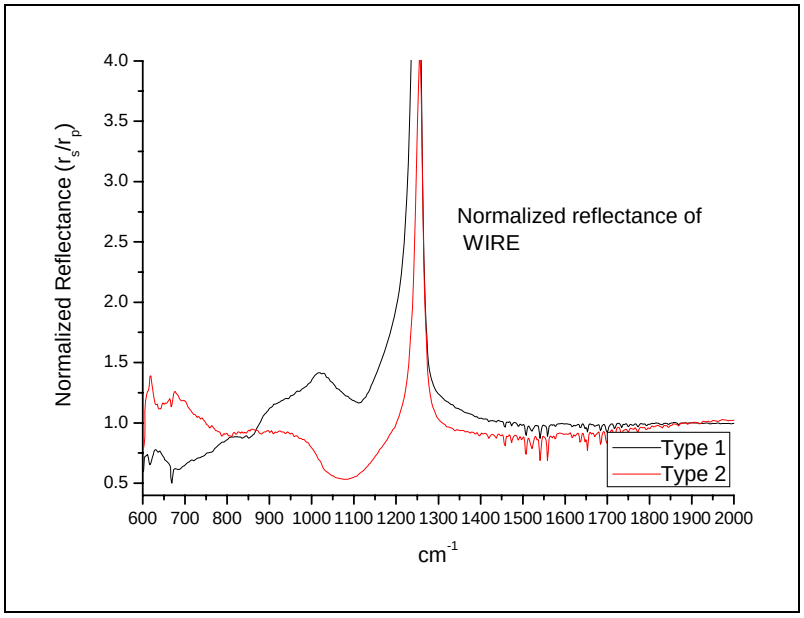

Figure 5-19. Type I and II arrangement of WIRE's normalized reflectance.

Discussion

Three major features are observed on Figure 5-19

1. k=1018.39cm^{-1} (f=30.55THz) for type I.

2. no obvious reflectance peak for type II.

3. k=1250cm^{-1} (f=37.5THz) exist for each type.(due to SiO_2)

For the discontinuous wire mesh structures, WIREs expect only one resonance according to the free electron model for permittivity. Another important characteristic is that discontinuous wire will have a relatively shorter range of stop-band, but continuous wire has very long range stop-band (theoretically, down to 0Hz frequency), like the dispersion model for free electrons. In this work, the measured spectrua, depicted that the reflectance peak was only observed in the case that the E field vector was parallel to short side of WIRE. When the E field vector was parallel to long side, no obvious reflection peak could be observed. This result may be explained by the fact that the resonance of that E field was parallel to short side would be higher than the case that E field was parallel to the long side. So the lower

resonance peak could not be observed since it might be lower than the detector limit of 600cm^{-1}.

5.3.3 Spectra of CMM

Step1. Reflectance

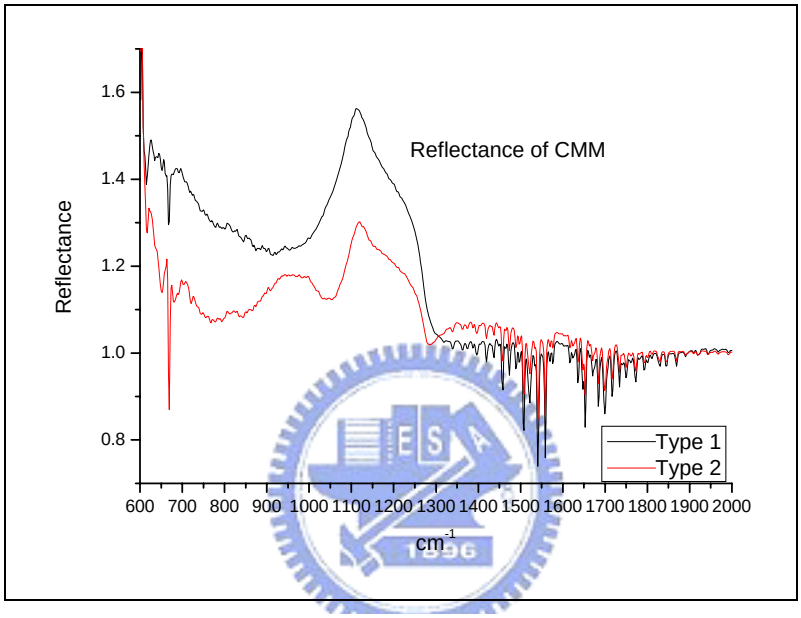

Figure 5-20. Type I and II arrangement of CMM's reflectance.

Step2. Normalized Reflectance

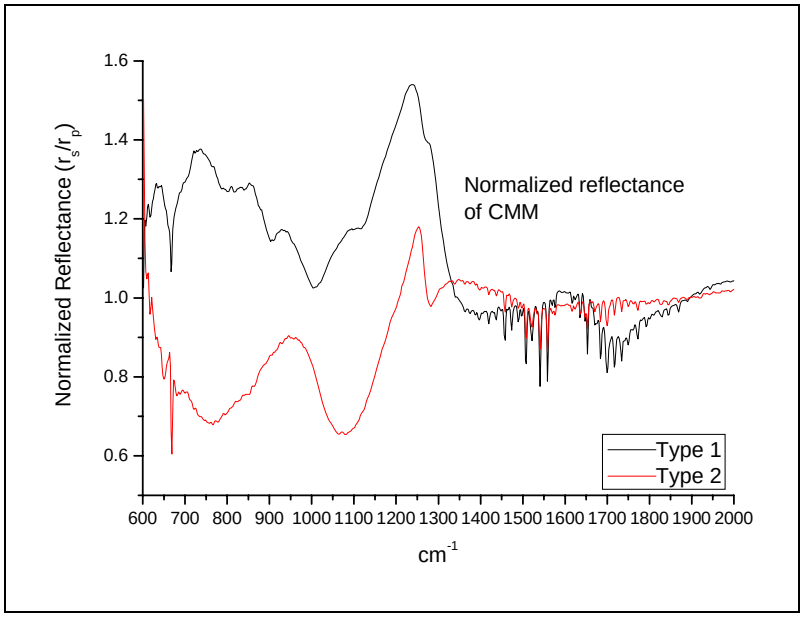

Figure 5-21. Type I and II arrangement of CMM's normalized reflectance.

Discussion

Three major features are shown in Figure 5-21

1. k=736.79cm^{-1} (f=22.10THz)、k=852.513cm^{-1} (f=25.58THz), and k=929.66cm^{-1} (f=27.89THz) for type I.
2. k=945.09cm^{-1} (f=28.35THz) for type II.
3. k=1250cm^{-1} (f=37.5THz) exist for each type. (due to SiO_2)

The SEM of CMM revealed that structural size of the SRR part was almost the same as the SRR only samples, but structure of WIRE appeared being failed. The design requested discrete wires, but they were continuous to a large extend. The linewidth of wires in CMM was also 0.123 um wider than WIRE. In type I arrangement, there were three interesting reflectance features at：k=736.79cm^{-1} (f=22.10THz)、k=852.513cm^{-1} (f=25.58THz)、k=929.66cm^{-1} (f=27.89THz). Spectra of type I CMM could be simply represented as a sum of spectra from type I-SRR and type I-WIRE. Figure 5-22 shows all three type I spectra for

comparison.

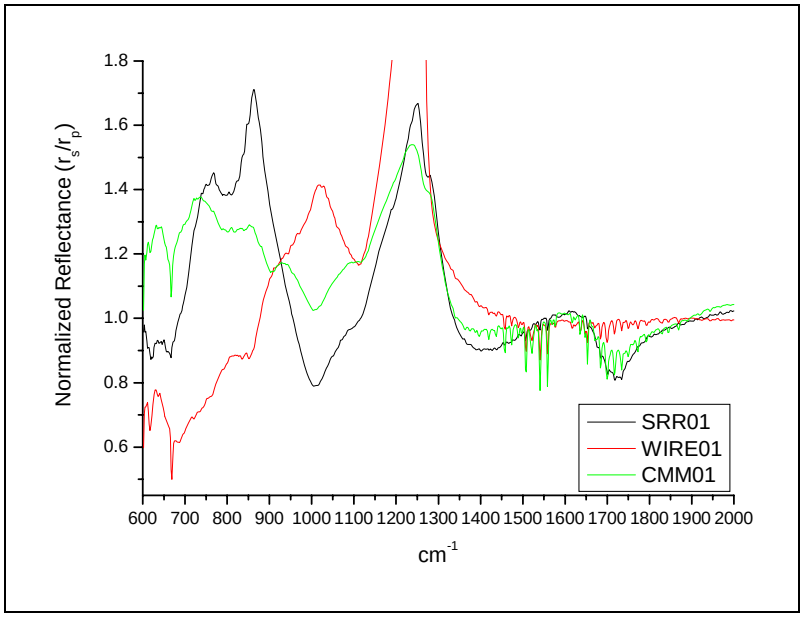

Figure 5-22. Normalized reflectance of three structures of type 1 arrangement.

In Figure 5-22, the first peak of CMM was basically the one due to the first peak of SRR but with a little red shift. The second peak of CMM was due to the second peak of SRR, and there was almost no difference in peak position. Third peak of CMM was speculated being due to continuous WIRE. Because the wires in CMM were continuous and wider, it consequently resulted in a red shift of peak.

In type II arrangement, there was only one interesting reflectance：k=945.09cm^{-1} (f=28.35THz). Spectra of type II CMM could again be represented as a sum of spectra from type II SRR and type II WIRE, as depicted in Figure 5-23.

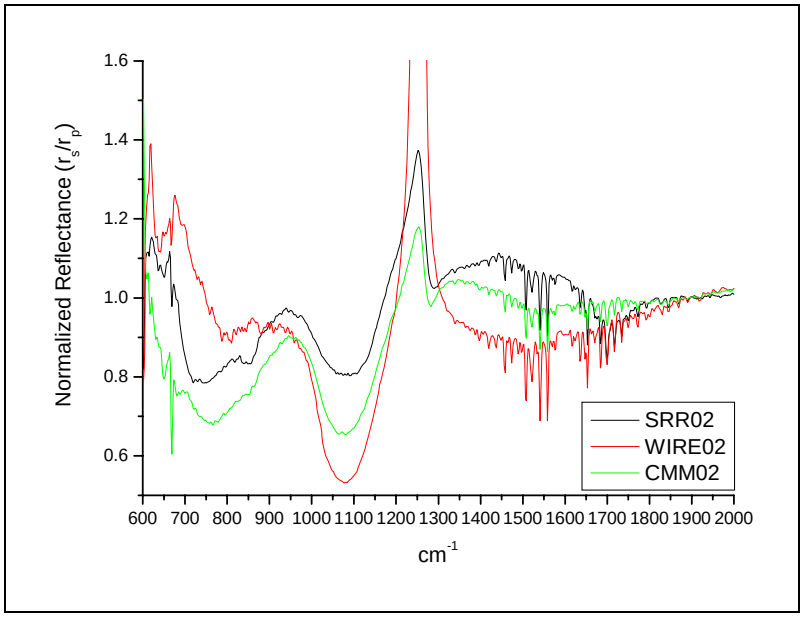

Figure 5-23. Normalized reflectance of three structures of type 2 arrangement.

While type II arrangement CMM didn't appear any specific spectral features, only one peak at k=945.09cm^{-1} (f=28.35THz) could be assigned due to reflectance. For type II arrangement of SRR and WIRE, the second peak of SRR appeared at k=941.24cm^{-1} (f=28.24THz) which was very close to tone measured at k=945.09cm^{-1} (f=28.35THz) of type II arrangement CMM. But the first peak of SRR was absent in type II CMM.

From above analyses, it could be concluded that for the designed CMM there was no observation of any negative refraction index in the mid-IR range. However, the effects of negative permittivity of discrete WIRE and negative permeability of SRR based on copper metallization and silicon substrate were successfully observed.

Chapter 6

Simulation results by CST

6.1 Introduction

In this chapter, simulation results obtained using Microwaves Studio, a computational tool provided by Computer Simulation Technology (CST) are presented for the comparison of experimental results. A simpler model was scotched than the situation of real experiments. No considerations of silicon dioxide, tantalum (adhesion layer), and residue of amorphous silicon were taken into account in the simulation scheme. The simulation structures were set to silicon substrate and patterns of copper metallization. The dispersion model of copper was drude model for which the plasma frequency was $1914*2\pi*10^{12}$ rad/s and collision frequency was $8.34*10^{12}$Hz. According to [52], the values of effective permittivity and permeability of meta-materials were derived from reflection and transmission coefficients. According to ref [52], there are following equations：

$$\varepsilon=n/z \tag{6.1}$$

$$\mu=nz \tag{6.2}$$

$$z=\pm\sqrt{\frac{(1+r)^2-t'^2}{(1-r)^2-t'^2}} \tag{6.3}$$

$$t'=\exp(ikd)t,\ k=\omega/c \tag{6.4}$$

$$\mathrm{Im}(n)=\pm\mathrm{Im}\left(\frac{\cos^{-1}\left(\frac{1}{2t'}[1-(r^2-t'^2)]\right)}{kd}\right) \tag{6.5}$$

$$\mathrm{Re}(n)=\pm\mathrm{Re}\left(\frac{\cos^{-1}\left(\frac{1}{2t'}[1-(r^2-t'^2)]\right)}{kd}\right)+\frac{2\pi m}{kd},\ m=\text{integer} \qquad \textbf{(6.6)}$$

6.2 Simulation results

6.2.1 Simulation results of SRR

The simulation results of SRR with different azimuths of light are presented in Figure 6-3. The definition of "Symmetry" means E field parallel to patterns of SRR and also parallel to symmetrical axis of SRR (shown as Figure 6-2), while "Asymmetry" means E field parallel to patterns of SRR and is orthogonal to symmetrical axis of SRR (shown as Figure 6-1). For simulations of SRR, H field was set normal to SRR, while E field and K were parallel to SRR. Port-1 was the excitation port to link the light source and port-2 was detection port. All E.M waves set as plane waves and boundary condition were maximum and minimum of x-plane =open, maximum and minimum of y-plane = E_t=0, maximum and minimum of z-plane = H_t=0. 4 SRR's cells were plotted for calculus. Thickness of copper was 50nm and silicon substrate was 200nm thick for setting up the simulation parameters.

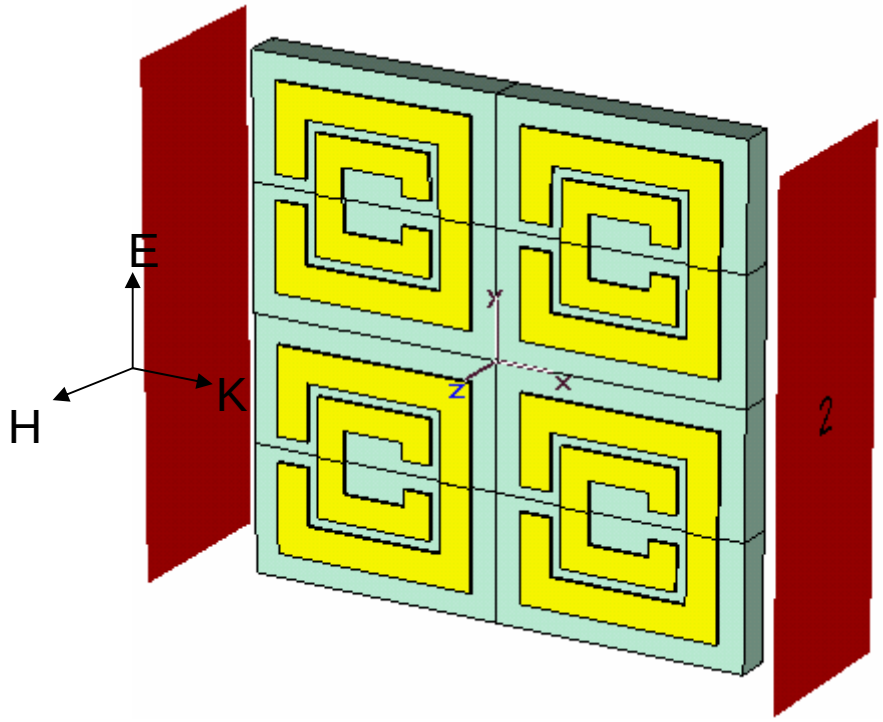

Figure 6-1 Diagram of E, H and K of asymmetrical incidence of SRR

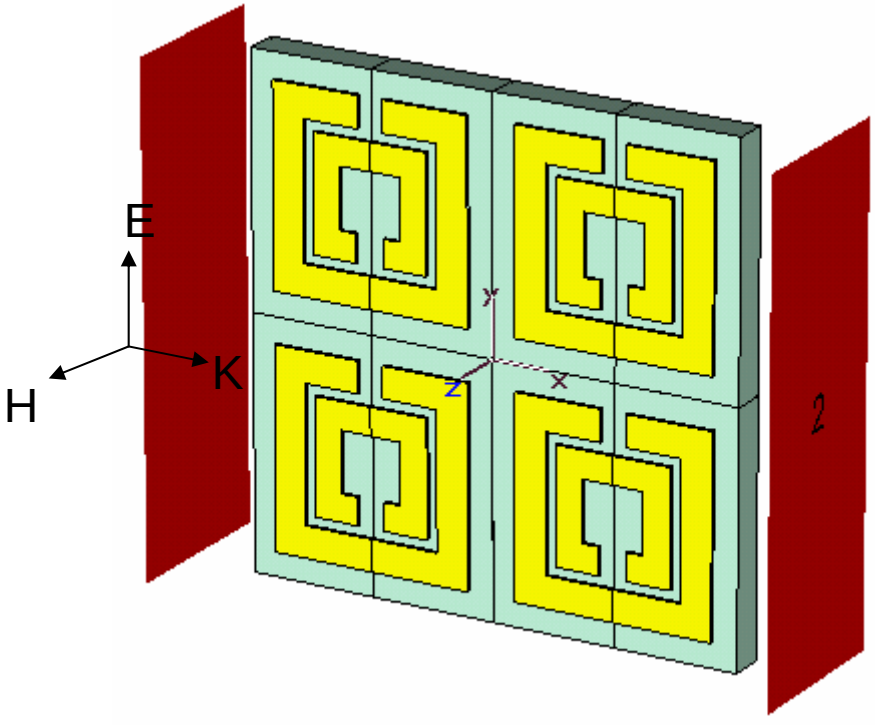

Figure 6-2 Diagram of E, H and K of symmetrical incidence of SRR

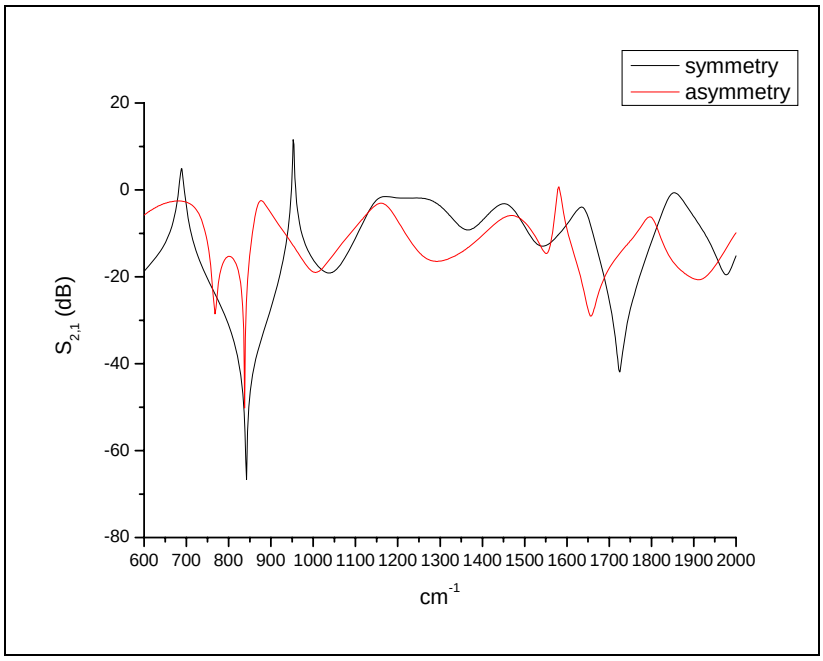

Figure 6-3 Simulation results of symmetrical and asymmetrical incidence of SRR

The derived permeability for different azimuths of SRR (i.e. symmetric or asymmetrical experimental geometries of SRR) are shown in Figures 6-4.and 6-5.

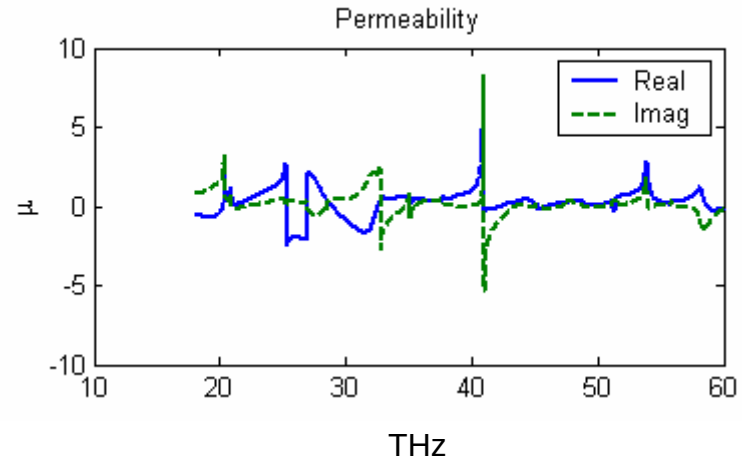

Figure 6-4 Permeability of symmetrical incidence of SRR

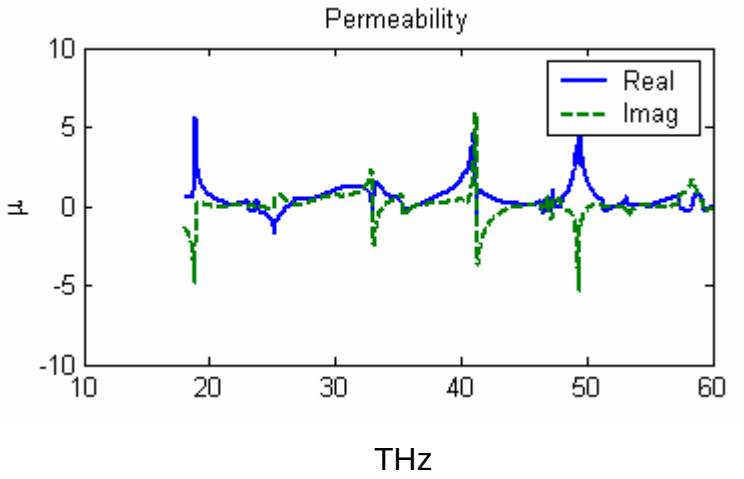

Figure 6-5 Permeability of asymmetrical incidence of SRR

From above results of simulation, transmission dips at $S_{2,1}$ at k=768cm^{-1} (f=23.04 THz) and k=838cm^{-1}(f=25.14THz) were observed for asymmetrical E field of SRR (i.e. corresponding to the type I arrangement of SRR), and at k=842cm^{-1}(f=25.26THz) for symmetrical E field of SRR (i.e. the type II arrangement of SRR).

In fact, Figures 6-4 and 6-5 are the conversion of transmission and reflection to permeability of two type arrangement of SRR. From the figures, both two types of SRR are shown to have the effect of negative permeability at a frequency range of approximately 23~26THz, i.e., k = 766.7 – 866.7 cm^{-1} that was in consistency with the experimental results.

Therefore, although the model structure for simulations was simpler, it still proved a quick and efficient mean for estimate. Simulations also explored that there were deeper and wider dips in the case of symmetrical E field of SRR, compared the results obtained for asymmetrical E field of SRR. This phenomenon was opposite to the report in ref [42], but it is a clear evidence that there is negative permeability in this Cu SRR patterns array in the mid-IR range.

Chapter 7

Conclusion

Meta-materials were studied in this thesis work, because their interesting “negative” optical properties. Three types of patterns, i.e., SRR, WIRE, and CMM were designed at the scale of ~200 nm, and were fabricated using a newly developed techniques, in which Cu patterns were made through Cu replacement reaction of Si backbone structures that were made by damascenes together with CMP. Optical measurements were then performed using FTIR for all three types of structure Below is a summary for all observations relating to those novel optical properties of Cu meta-materials：

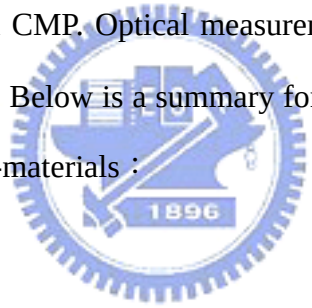

1. SRR

The spectra of normalized reflectance of two arrangements of SRR showed somer interesting results for optical measurement in Figure 5-17. In type I arrangement, there are two reflection peaks at k=767.6cm^{-1}(f=23.028THz) and k=864cm^{-1} (f=25.92THz), respectively. In type II arrangement, two peaks were observed at k=825.51cm^{-1} (f=24.77THz) and k=941.24cm^{-1} (f=28.24THz). At K=1250cm^{-1} (f=37.50THz) there exists a strong reflection feature in all spectra, which has been assigned due to interference of residual silicon dioxide layer. In chapter 6 for simulations, we have obtained simulation results：For Figure 6-1 (asymmetry, similar to type I arrangement), there were two $S_{2,1}$ dips at k=838cm^{-1} (f=25.14THz) and k=768cm^{-1} (f=23.04THz). For Figure 6-2 (symmetry, similar to type II arrangement), there was only one dip at k=842.20cm^{-1} (f=25.27THz) (but it has wide range for

$S_{2,1}$ dip.)

Therefore, the observed features could be assigned due to the effect of negative permeability in the SRR sample made of Cu metallization and silicon substrate.

2. WIRE

For WIRE patterns, only one feature at k=1018.39cm^{-1} (f=30.55THz) was observed in the reflection spectrum for the measurement arrangement of type I. No obvious features could be assigned to the enhanced reflectance because there exists no resonance the the spectrum for the experiment with a type II arrangement,

So, one can conclude that the effect of negative permittivity of discrete WIRE was successfully observed.

3. CMM

For the type I arrangement, there were three interesting reflectance features at k=736.79cm^{-1} (f=22.10THz)、k=852.51cm^{-1} (f=25.58THz), and k=929.66cm^{-1} (f=27.89THz), respectively. Noted that two of these three (i.e. k=736.79cm^{-1} (f=22.10THz) 、k=852.51cm^{-1} (f=25.58THz)) were similar to those observed from the sample with only patterns of SRR, while both have little peak shift to lower wavenumber.

For the type II arrangement, there was only one distinct feature at k=945.09cm^{-1} (f=28.35THz). Compared to the experiments with the type II arrangement of SRR and WIRE, only SRR showed a reflectance peak at k=941.24cm^{-1} (f=28.24THz), which is close to the feature of type II arrangement CMM (k=945.09cm^{-1} (f=28.35THz) in term of the wavenumber position). But the first peak of SRR was absent in type II CMM. Therefore, no conclusion could be made whether there was any feature due to negative refraction index in the mid-IR range.

Reference

[1] V. G. Veselago, “The electrodynamics of substance with simultaneously negative values of ε and μ”, *Sov. Phys. Usp.*, vol. 10, pp. 509, 1968.

[2] J. B. Pendry, A. J. Holden, W. J. Stewart and I. Youngs, “Extremely low frequency plasmons in metallic mesostructures”, *Phys. Rev. Lett.*, vol. 76, pp. 4773, 1996.

[3] J. B. Pendry, A. J. Holden, D. J. Robbins and W. J. Stewart, “Magnetism from conductors and enhanced nonlinear phenomena”, *IEEE Trans. Microwave Theory and Tech.*, vol. 47, pp. 2075, 1999.

[4] D. R. Smith , W. J. Padilla, D. C. Vier, S. C. Nemat-Nasser and S. Schultz, “Composite medium with simultaneously negative permeability and permittivity“, *Phys. Rev. Lett.*, vol. 84, pp. 4184, 2000.

[5] R. A. Shelby, D. R. Smithand S. Schultz, “Experimental Verification of a Negative Index of Refraction”, *Science*, vol. 292, pp. 77, 2001.

[6] J. B. Pendry, “Negative refraction”, *Contemp. Phys.*, vol. 45, pp. 191, 2004.

[7] J. T. Shen and P. M. Platzmann, “Near field imaging with negative dielectric constant lenses”, *Appl. Phys. Lett.*, vol. 80, pp. 3286, 2002.

[8] S. A. Ramamkrishna, ”Physics of negative refractive index materials”, *Rep. Prog. Phys.*, vol. 68, pp. 449-521, 2005.

[9] J. B. Pendry, A. J. Holden, D. J. Robbins and W. J. Steward, ”Low frequency plasmons in thin-wire structures”, *J. Phys.: Condens. Matter*, vol. 10, pp. 4785, 1998.

[10] D. F. Sievenpiper, M. E. Sickmiller and E. Yablonovitch, ”3D Wire mesh photonic crystals”, *Phys. Rev. Lett.*, vol. 76, pp. 2480, 1996.

[11] C. G. Parazzoli, R. B. Greegor, K. Li, B. E. C. Kontenbah and M. H. Tanielian, “Experimental verification and simulation of negative index of refraction using snell’s law”, *Phys. Rev. Lett.*, vol. 90, pp. 107401,2003.

[12] K. Li, S. J. McLean, R. B. Greegor, C. G. Parazzoli and M. H. Tanielian, ” Free-space focused-beam characterization of left-handed materials”, *Appl. Phys. Lett.*, vol. 82, pp. 2535, 2003.

[13] T. J. Yen, W. J. Padilla, N. Fang, D. C. Vier, D. R. Smith, J. B. Pendry, D. N. Basov and X. Zhang, “Terahertz magnetic response from artificial materials”, *Science*, vol.

303, pp. 1494, 2004.

[14] P. Gay-Balmaz and O. J. F. Martin, "Electromagnetic resonances in individual and coupled split-ring resonators", *J. Appl. Phys.*, vol. 92, pp. 2929, 2002.

[15] P. Gay-Balmaz and O. J. F. Martin, "Efficient isotropic magnetic resonators", *Appl. Phys. Lett.*, vol. 81, pp. 939, 2002.

[16] M. C. K. Wiltshire, J. B. Pendry, I. R. Young, D. J. Larkman, D. J. Gilderdale and J. V. Hajnal, "Microstructured magnetic materials for RF flux guides in magnetic resonance imaging", *Science*, vol. 291, pp. 849, 2001.

[17] M. C. K. Wiltshire, J. V. Hajnal, J. B. Pendry and D. J. Edwards, "RF field transmission through swiss rolls – an anisotropic magnetic metamaterial", *Opt. Express*, vol. 11, pp. 709, 2003.

[18] L. V. Panina, A. N. Grigorenko and D. P. Makhnovskiy, "Optomagnetic composite medium with conducting nanoelements", *Phys. Rev.* B, vol. 66, pp. 155411, 2002.

[19] S. Hrabar , J. Bartolic, Z. Eres, "Capacitively Loaded Loop as Basic Element of Negative Permeability Meta-material", 32nd European Microwave Conference Proceedings, pp. 327-330, Milan, Italy, 24-26 September 2002.

[20] E. Shamonina, V. A. Kalinin, K. H. Ringhofer and L. Solymar, "Magnetoinductive waves in one, two, and three dimensions", *J. Appl. Phys.*, vol. 92, pp. 6252, 2002.

[21] M. Shamonin, E. Shamonina, V. Kalinin and L. Solymar, "Properties of a metamaterial element: Analytical solutions and numerical simulations for a singly split double ring", *J. Appl. Phys.*, vol. 95, pp. 3778, 2004.

[22] M. M. I. Saadoun and N. Engheta, "A reciprocal phase shifter using novel pseudochiral or ω medium", *Microwave Opt. Tech. Lett.*, vol. 5, pp. 184, 1992.

[23] C. R. Simovsky and S. He, "Frequency range and explicit expressions for negative permittivity and permeability for an isotropic medium formed by a lattice of perfectly conducting Ω particles", *Phys. Lett.* A, vol. 311, pp. 254, 2003.

[24] R. Marques, F. Medina and R. Rafii-El-Idrissi, "Role of bianisotropy in negative permeability and left-handed metamaterials", *Phys. Rev.* B, vol. 65, pp. 144440, 2002.

[25] P. Gay-Balmaz and O. J. F. Martin, "Electromagnetic resonances in individual and coupled split-ring resonators", *J. Appl. Phys.*, vol. 92, pp. 2929, 2002.

[26] Koray Aydin, Irfan Bulu, Kaan Guven, Maria Kafesaki, Costas M Soukoulis, and Ekmel Ozbay, “Investigation of magnetic resonances for different split-ring resonator parameters and designs”, *New Journal of Physics*, vol. 7, pp. 168, 2005.

[27] T. J. Yen, W. J. Padilla, N. Fang, D. C. Vier, D. R. Smith, J. B. Pendry, D. N. Basov and X. Zhang, “Terahertz magnetic response from artificial materials”, *Science*, vol. 303, pp.1494, 2004.

[28] S. Linden, C. Enkrich, M. Wegener, J. Zhou, T. Koschny and C. M. Soukoulis, “Magnetic Response of Metamaterials at 100 Terahertz”, *Science*, vol. 306, pp. 1351, 2004.

[29] N. Katsarakis, T. Koschny, M. Kafesaki, E. N. Economou and C. M. Soukoulis, “Electric coupling to the magnetic resonance of split ring resonators”, *Appl. Phys. Lett.*, vol. 84, pp. 2943, 2004.

[30] R. A. Shelby, D. R. Smith, S. C. Nemat-Nasser and S. Schultz, “Microwave transmission through a two-dimensional, isotropic, left-handed metamaterial ”, Appl. Phys. Lett., vol. 78, pp. 489, 2001.

[31] Ekmel Ozbay, Koray Aydin, Ertugrul Cubukcu, and Mehmet Bayindir, “Transmission and reflection properties of composite double negative metamaterials in free space“, IEEE transactions on antennas and propagation, vol. 51, no. 10, pp. 2592-2595, OCTOBER 2003.

[32] D. R. Smith and N. Kroll, “Negative refractive index in left-handed materials,” *Phys. Rev. Lett.*, vol. 85, no. 14, pp. 2933–2936, Oct. 2000.

[33] M. Bayindir, K. Aydin, E. Ozbay, P. Markos, and C. M. Soukoulis, “Transmission properties of composite metamaterials in free space,” *Appl. Phys. Lett.*, vol. 81, no. 1, pp. 120–122, July 2002.

[34] R. A. Shelby, D. R. Smith, S. C. Nemat-Nasser, and S. Schultz, “Microwave transmission through a two-dimensional, isotropic, left-handed metamaterial,” *Appl. Phys. Lett.*, vol. 78, no. 4, pp. 489–491, Jan. 2001.

[35] R. W. Ziolkowski and E. Heyman, “Wave propagation in media having negative permittivity and permeability,” *Phys. Rev. E*, vol. 64, no.056 625, pp. 1–15, Oct. 2001.

[36] D. R. Smith, S. Schultz, P. Markos, and C. M. Soukoulis, “Determination of

permittivity and permeability of metamaterials from scattering data," *Phys. Rev. B*, vol. 65, no. 195 104, May 2002.

[37] P. Markos, I. Rousochatzakis, and C. M. Soukoulis, "Transmission losses in left-handed materials," *Phys. Rev. E*, vol. 66, no. 045 601, Oct. 2002.

[38] H. O. Moser,B. D. F. Casse, O. Wilhelmi, and B. T. Saw, "Terahertz response of a microfabricated rod–split-ring-resonator electromagnetic metamaterial", *phys. Rev. let*., vol. 94, pp. 063901, 2005.

[39] S. Roberts, "Optical properties of copper", *phys. rev.*, vol. 118, no. 6, june 15,1960.

[40] N. Katsarakis, T. Koschny, and M. Kafesaki, E. N. Economou, C. M. Soukoulis, "Electric coupling to the magnetic resonance of split ring resonators", *App. Phys. Let.*, vol. 84, pp. 2943, 2004.

[41] T. Koschny, M. Kafesaki, E. N. Economou, and C. M. Soukoulis, "Effective medium theory of left-handed materials", Phys. Rev. Lett., vol. 93, pp. 107402, 2004.

[42] N. Katsarakis, T. Koschny, and M. Kafesaki, E. N. Economou, C. M. Soukoulis, "Electric coupling to the magnetic resonance of split ring resonators", *App. Phys. Let.*, vol. 84, pp. 2943, 2004.

[43] S. I. Maslovsky, S. A. Tretyakov and P. A. Belov, " Wire media with negative effective permittivity: A quasi-static model", *Microwave Opt. Tech. Lett.*, vol. 35, pp. 47, 2002.

[44] H. Raether, "Excitation of plasmons and interband transitions by electrons", *Applied Optics IP*, vol. 20, no. 20, pp. 3588 , 1980.

[45] Yin-Ping Lee, Ming-Shih Tsai, Ting-Chen Hu, Bau-Tong Dai, and Ming-Shiann Fenga, "Selective copper metallization by electrochemical contact displacement with amorphous silicon film", *Electrochemical and Solid-State Letters*, vol. 4, no. 7, pp. C47-C49, 2001.

[46]. G. Li, E. A. Kneer, B. Vermeire, H. G. Parks, and S. Raghavan, "A comparative electrochemical study of copper deposition onto silicon from dilute and buffered hydrofluoric acids", *J. Electrochem. Soc.,* vol. 145, pp. 241, 1998.

[47]. B. Zhao, P. K. Vasudev, and C. H. Ting, "Selective and blanket electroless Copper deposition for ultralarge scale integration", *J. Electrochem. Soc.,* vol.144, pp.898,

1997.

[48]. Y. Shacham-Diamand and S. Lopatin, “Integrated electroless metallization for ULSI”, *Electrochim. Acta,*vol. 44, pp.3639, 1999.

[49]. G. J. Norga, M. Platero, K. A. Black, A. J. Reddy, J. Michel, and L. C. Kimerling, “Mechanism of copper deposition on silicon from dilute hydrofluoric acid solution”, *J. Electrochem. Soc.,* vol. 144, pp.2801,1997.

[50]. M. K. Lee, J. J. Wang, and H. D. Wang, “Deposition of copper films on silicon from cupric sulfate and hydrofluoric acid”, *J. Electrochem. Soc.,* vol. 144, pp.1777, 1997.

[51] M. K. afesaki, T. Koschny, R. S. Penciu, T. F.Gundogdu, E. N. Economou and C M Soukoulis, “Left-handed metamaterials: detailed numerical studies of the transmission properties”, *J. Opt. A: Pure Appl. Opt.*, vol. 7, pp. S12–S22, 2005.

[52] D. R. Smith and S. Schultz, P. Markos and C. M. Soukoulis, “Determination of effective permittivity and permeability of metamaterials from reflection and transmission coefficients”, *phys. rev. B*, vol. 65, pp. 195104, 2002.

Curriculum Vita

Pei-Hsuan Han was born in Taipei, Taiwan, on October 10, 1983. He received the B.S. degree in Physics from National Central University (NCU) in June 2005. He entered the Institute of Electronics, National Chiao Tung University (NCTU), in September 2005. His major study was meta-materials. He received the M.S. degree from NCTU in August 2007.